Defects and Transport in RE_2WO_6

Master thesis in Materials, Energy and Nanotechnology

by Jie Pan

Centre for Materials Science and Nanotechnology

Department of Chemistry

University of Oslo

Preface

This thesis presents the work done for a Master's degree in Material, Energy and Nanotechnology, department of chemistry, Univeristy of Oslo. This work was carried out in FERMiO at SMN from August 2010 to June 2012.

Firstly, I feel obliged to express my thanks to Professor Truls Norby, who gave me the opportunity to work with proton conductors.

And I should thank my supervisor Dr. Reidar Haugsrud and co-supervisor Dr. Zuoan Li, who offered lots of valuable suggestion in experiments.

I also thank Harald Fjeld, Ragnar Strandbakke, Camilla Vigen, Anna Magrasó, Liv Elisif Q Kalland for the experimental methods teaching and suggestions for experimental set up.

Finally, I would like to thank my officemate Wen Xing, with whom lots of interesting questions are discussed.

University of Oslo

May 2012

Jie Pan

List of acronyms and symbols

A*	Admittance
a_X	Activity of a component X
AC	Alternating current
b	Bulk
BSE	Back-scattered electron
DC	Direct current
CPE	Constant phase element
E_a	Activation energy
EDS/EDX	Energy dispersive X-ray spectroscopy
EDTA	Ethylenediaminetetraacetic acid
EIS	Electrochemical impedance spectroscopy
EMF	Electromotive force
F	Faraday's constant
FC	Fuel cell
FEG	Field emission gun
gb	Grain boundary
HTPC	High temperature proton conductor
HT-PCFC	High-temperature proton conducting fuel cell
K_{eq}	Equilibrium constant
L	Inductive element
OCV	Open circuit voltage
p	Electron hole concentration
p_{H_2O}	Water vapor partial pressure
p_{O_2}	Oxygen partial pressure
PCFC	Proton conducting fuel cell

R	Resistance/Gas constant
R_b	Bulk resistance
R_{gb}	Grain boundary resistance
R_e	Electrode resistance
powder XRD	Powder X-ray diffraction
SEM	Scanning electron microscope
SOFC	Solid Oxide Fuel Cell
T	Temperature
t_i	Transport number of species i
$Z^{|}$	Real part of the complex impedance
$Z^{||}$	Imaginary part of the complex impedance
ΔH	Enthalpy
ΔH_{hyd}	Enthalpy of the reaction of hydration of oxygen vacancies
ΔH_m	Activation enthalpy of migration
ΔG	Gibbs free energy
ΔS	Entropy
E^*	Permittivity
σ	Conductivity

Table of contents

1. Introduction

1.1 Renewable energy

Energy consumption has always been playing an important role in human society, fundamentally in individuals' daily life as well as national or international commercialized industries on a bigger scale. It is the lifeblood of modern economies which always have influence on every individual as well as international company.

However, with the fast development of economies and technologies, more and more energy are demanded. Thus human have to burn more and more coal and oil or try to develop renewable energies to meet their increasing demands.

Since the 19th century, several modern types of technologies for sustainable energy have been developed including solar energy, wind energy, hydro electric power and etc.. These technologies are only used in a very small scale due to the higher prices than the fossil based energy.

Fuel cell technology developed in recent decades is one of the most promising candidates in future energy conversion technology. Although the cost per KW generated is higher than other technologies at the moment, it has been calculated that the conversion efficiency of a Solid Oxide Fuel Cell (SOFC) is estimated around 60% and makes it higher than 40% of a traditional combustion engine. As a plus, the SOFC technology is almost a clean energy conversion process.

Thus, such kind of clean, renewable technologies is necessary to be developed in spite of the higher cost per KW before it becomes mature and available for commercialization and used on a big scale. One of the significant challenges for the development of SOFCs is the insufficient ionic conductivity of the solid oxide electrolytes which limits the energy conversion efficiency. Finding better materials for solid electrolytes would help to achieve greater progresses for the development of SOFC technology.

SOFCs are mainly divided into oxygen ion conducting and proton conducting SOFCs, according to the predominant conducting ions. Oxygen ion conducting SOFCs already have been commercialized by Bloom energy for the production of Energy Servers as distributed power generators. While, the peak conductivity of the best proton conducting material ever discovered is approximately 0.01S/cm which is by one order of magnitude lower than that of

best oxygen ion conducting material. Thus, projects have been set up aiming at discovering proton conducting materials with higher conductivity.

1.2 Solid oxide fuel cells (SOFCs)

Solid oxide fuel cells (SOFCs) are energy conversion devices that produce electricity directly from a gaseous fuel by electrochemical combination of the fuel with an oxidant without combustion. The advantages of SOFCs compared to conventional electric power generation systems are higher conversion efficiency and more environmental compatibility, both of which are important in today's society.

In traditional oxygen ion conducting SOFCs, oxygen (from air) is reduced by a porous electrode (cathode) producing oxide ions which migrate through a pure oxygen ion conducting oxide as solid electrolyte to the porous fuel electrode (anode) and react with the fuel (H_2, CO, CH_4) forming H_2O and/or CO_2.

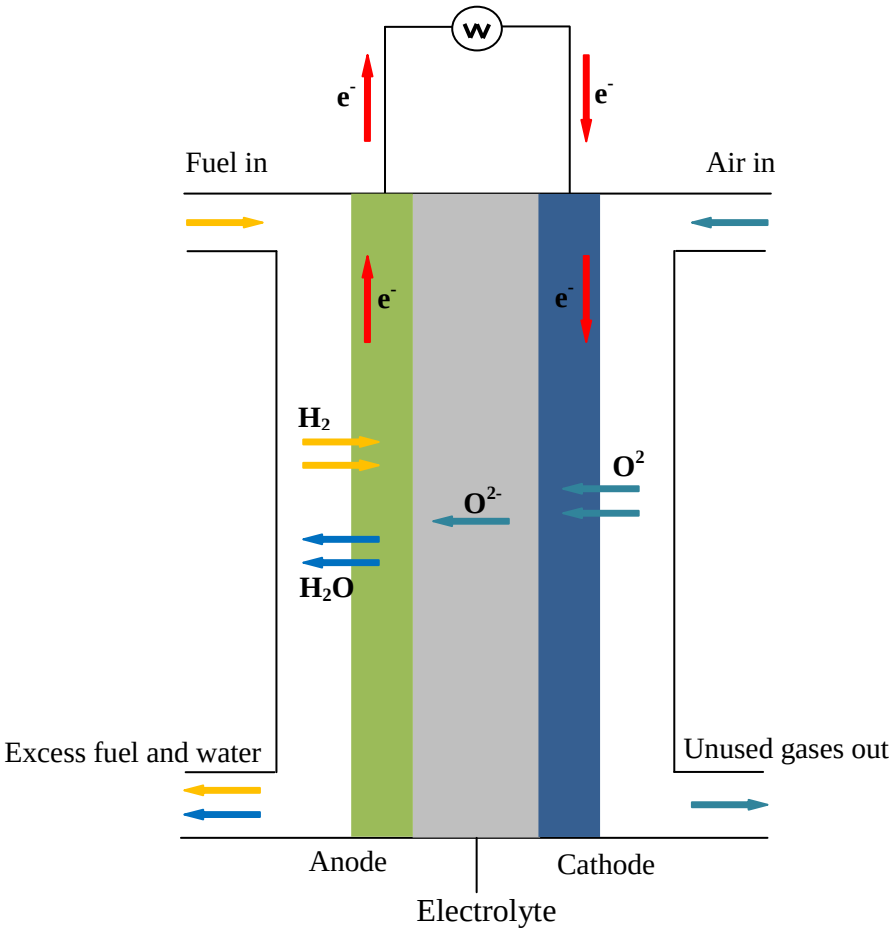

Figure 1-1 Scheme of an oxygen ion conducting SOFC

Partial reactions at the anode and cathode:

Anode:

$$H_2(g) + O^{2-} \rightarrow H_2O(g) + 2e^- \quad (1\text{-}1)$$

Cathode:

$$\frac{1}{2}O_2(g) + 2e^- \rightarrow O^{2-} \quad (1\text{-}2)$$

In turn, a proton conducting solid electrolyte can be used, where H_2 is oxidized to produce protons that subsequently migrate through electrolyte and react with oxygen to form water at the cathode side. The operation principle in such a proton conductor based fuel cell (PCFC) is schematically shown in the figure below.

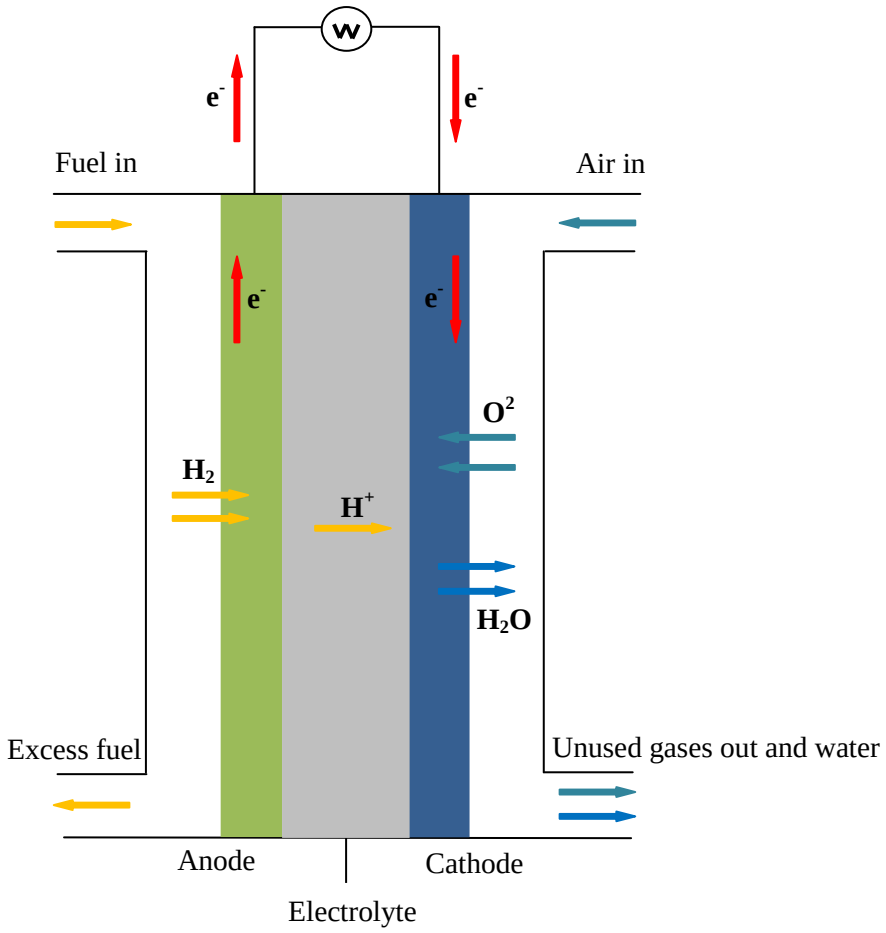

Figure 1-2 Scheme of the proton conducting fuel cell (PCFC)

Partial reactions at the anode and cathode:

Anode:

$$H_2(g) \rightarrow 2H^+ + 2e^- \tag{1-3}$$

Cathode:

$$\frac{1}{2}O_2(g) + 2e^- + 2H^+ \rightarrow H_2O \tag{1-4}$$

One could see that, in a traditional oxygen ion conducting fuel cell, water forms on the feed side and dilutes the fuel concentration which limits the efficiency of energy conversion. On the other hand, in a PCFC, water forms and leaves the system on the side exposed to air. Based on the big advantage over traditional oxygen ion fuel cell, PCFC technology is developed.

1.3 Proton conductors

Since the discovery of proton conductivity in ice more than a hundred years ago in Japan, proton conduction in solids has become of considerable interest. Projects have been set up for researches on proton conductors and as with many other ionic conductors, for they can be used in kinds of electrochemical devices such as fuel cells, separation membranes, super capacitors, chemical sensors, eletrochromic displays and etc. [1].

So far, several proton-conducting oxides have been discovered, with conductivities peaking at approximately 1×10^{-2} S/cm for perovskite structured alkaline earth cerates and zirconates. The disadvantage with these materials is the basic character of the alkaline-earths, which makes them reactive with acidic gases like CO_2, and, therefore, vulnerable towards degradation. State-of-the-art high temperature proton conductors meeting the stability requirements unfortunately have conductivities at least one order of magnitude lower than the perovskites [1]. Conductivities in the order of 1×10^{-3} S/cm will require thin films to be applied in high-drain energy technologies such as solid electrolytes in fuel cells.

1.4 RE_2WO_6 as potential proton conductors

As mentioned earlier, there are some of materials as potential proton conductors with satisfying proton conductivity. One of the classes of materials that come out with relatively

high score from these evaluations is the rare earth tungstates ($RE_XW_YO_Z$). These tungstates form a group of ceramic materials with numerous stoichiometries whose functional properties are dependent upon the crystalline structure and on the valence of tungsten. So far, only one or two compositions (different X-Y ratio) within this series have been characterized with respect to the ionic transport properties emphasizing on effects of protons. It has been shown that Ln_6WO_{12} exhibits interesting transport properties[2-4], and La_6WO_{12} (the stoichiometry was modified as $La_{5.3\text{-}5.7}WO_{12-\delta}$ based on later research[5, 6]) based materials reach proton conductivities in the order of 3×10^{-3} S/cm at approximately 800°C[4].

A related compound also with tungsten in valence state of +6, La_2WO_6 is of interest. The structure of the low-temperature form of β-La_2WO_6 has been determined from laboratory X-ray, neutron time-of-flight and electron diffraction data. The structure consists of octahedral [WO_6] and tetrahedral [OLa_4] [7].

1.5 Aim of this work

The aim of this work is to characterize the defect structure and transport properties of materials within the Ln_2WO_6 (Ln=La, Gd and Er) class of materials, nominally undoped as well as A-site acceptor substituted derivatives (A=Ca or Sr).

More specifically measurements of the electrical conductivity and the stoichiometry of the materials will serve as the bases to derive defect chemical models from which physicochemical constants of the different materials can be extracted. These include the standard molar enthalpy and entropy associated with dissolution of protons (hydration), the preexponential and enthalpy of mobility for the different charge carriers. Attempts will be made to rationalize the variation of these parameters along the series of the materials based on changes in structural parameters.

2. Theory

2.1 Defects in oxides and Kröger-Vink notation

Chemists believed that the composition in crystals are definite and stoichiometric until 1930s, when Wagner and Schottky demonstrated that structures are not ideal based on their work and different forms of structural defects could exist in a crystal:

(1) Point defects: imperfections in the crystal lattice which are limited into a specific positions and their immediate vicinity, they could exist in the crystal structure in forms of vacancies, interstials, substitutionals (from inner or external ions);

(2) Dislocations: linear defects around which some of the atoms of the crystal lattice are misaligned;

(3) Planar defects: stacking faults, so-called shear planes or internal and external surfaces;

(4) Bulk defects: voids and impurities.

In addition, crystals could also contain electronic defects such as electrons and electron holes.

Defects will be described by so-called Kröger-Vink notation in this work. In this system, the reference structure has a constant ratio between the numbers of the structural sites of the different components of the materials. Thus, for instance, in a metal oxide MO, the ratio of structural metal sites to oxygen sites is constant and equal to 1:1. Furthermore, the valence of the ions, M^{2+} and O^{2-}, are used as the reference of the metal and oxygen sites. If an oxygen ion on a structural oxygen site has a valence of -1, there is an electron hole localized at this particular site, this oxygen site will have an "effective" charge of +1.

Furthermore, if an oxygen atom is removed from its site together with the two electron then the remaining oxygen vacancy will have two effective positive charge. Some examples of the Kröger-Vink notation are given below:

$O_{\mathrm{O}}^{\mathrm{X}}$ A normal oxygen ion on a normal oxygen site.

$M_{\mathrm{M}}^{\mathrm{X}}$ A normal metal ion on a normal metal site.

$v_O^{\bullet\bullet}$ An oxygen vacancy with two effective charges.

$v_M^{///}$ A metal vacancy with three effective negative charges.

$M_i^{\bullet\bullet\bullet}$ An interstial metal ion with three effective positive charges.

$H_i^{\bullet}$ An interstial proton with one effective positive charge.

$O_i^{//}$ An interstial oxygen ion with two effective negative charges.

$O\mathrm{H}_O^{\bullet}$ A hydroxide ion on a oxygen site with one positive charge.

$M\mathrm{f}_M^{/}$ A foreign metal ion on a metal site with one effective negative charge.

From these examples, it is seen that the major symbol refers to the type of defects; the subscript refers to the site and the super script to the effective charge of the defect. Furthermore, electronic defects are denoted by e^- for electron and $h^{\cdot}$ for electron holes.

Reactions involving defects can be written in terms of defect equations, and their concentrations through corresponding defect equilibria. Concentrations of point defects are denoted by brackets, for instance $[V_O^{\cdot\cdot}]$, electrons by n and electron holes by p. In these terms, the Frenkel and anti-Frenkel reactions in an oxide as MO could be written as:

$$M_M^X = M_i^{\bullet\bullet\bullet} + V_M^{///} \tag{2-1}$$

$$O_O^X = v_O^{\bullet\bullet} + O_i^{//} \tag{2-2}$$

The corresponding mass action expressions could be written as:

$$K_F = [M_i^{\bullet\bullet\bullet}][V_M^{///}] \tag{2-3}$$

$$K_{AF} = [v_O^{\bullet\bullet}][O_i^{//}] \tag{2-4}$$

Where K_F and K_{AF} are equilibrium constants. The fractions of metal and oxygen ions, $[M_M^X][O_O^X]$, are usually set equal to unity for systems with low defect concentrations.

When defect reactions are written, three rules should be followed: (1) Conservation of mass; (2) Conservation of charge; (3) Conservation of the ratio of structure sites.

2.2 Thermodynamics of defects

Thermodynamically, no defect could exist at 0 K in a material. In all crystalline materials above 0K, a specific concentration of defects is thermodynamically stable. This may be related to the entropy of the system and the enthalpy of formation of defects by applying dilute solution theory with the crystal as solvent and defects as solute.

The formula for Gibbs free energy for the system is :

$$\Delta G = \Delta H - T\Delta S \tag{2-5}$$

Where ΔH is the change in enthalpy per defect introduced in the crystal, and ΔS is the change in configurational entropy and T is the temperature. ΔH increases linearly with increasing defect concentration. ΔS also increase with increasing defect concentration according to Boltzmann's formula for entropy.

$$S = k \ln W \tag{2-6}$$

Where k is Boltzmann's constant and W is the weight of the configuration of the system.

$$\frac{\partial G}{\partial x} = 0 \tag{2-7}$$

Where x is the concentration of defects. Thus the minimum represents the thermodynamically stable concentration at a specified temperature. The enthalpy of formation of defects is usually positive, because it normally requires energy to produce the defects. The change in entropy is also positive because the defects introduce disorder in an ordered system.

By increasing the temperature the TΔS part becomes more dominating. Thus the minimum is displaced to higher defect concentrations and the thermodynamically stable concentration of defects increases with increasing temperature.

2.3 Assumed defects in La_2WO_6

Defects in stoichiometric La_2WO_6

A stoichiometric oxide is an oxide where the concentrations of anion and cation defects are equivalent. Schottky and Frenkel disorders do not change the stoichiometry of an oxide. A

Schottky disordered oxide has equivalent concentrations of cation and anion vacancies. For an oxide like La_2O_3 this means the simultaneous presence of lanthanum and oxygen vacancies.

$$0 = 3V_O^{\bullet\bullet} + 2V_{La}^{///} \tag{2-8}$$

The reaction forms two new metal sites and three new oxygen sites.

An important aspect of Schottky disorders is that they are formed on surfaces, and then has to diffuse in to the bulk of the material until equilibrium is established. Thus equilibration of Schottky disordered oxides may be slow due to this diffusion process.

A Frenkel disordered oxide has equivalent concentrations of cation interstitials and vacancies for the same atom. To make a Frenkel disorder in La_2O_3 a lanthanum jumps to an interstitial site, leaving a vacancy.

$$La_{La}^{X} = La_i^{\bullet\bullet\bullet} + V_{La}^{///} \tag{2-9}$$

Defects in Non-stoichiometric La_2WO_6

Non-stoichiometric oxides on the other hand have defect concentrations that change the stoichiometry of the oxide. For instance of the oxide has more oxygen vacancies than metal vacancies, the oxide is oxygen deficient. Oxides that have more metal vacancies than oxygen vacancies are metal deficient.

When the oxide has an excess of one type of defect, then the oxide is non-stoichiometric. Non-stoichiometry in oxides depends on the oxygen partial pressure as exemplified for La_2WO_6.

$$O_O^X = v_O^{\bullet\bullet} + \frac{1}{2}O_2 \tag{2-10}$$

By doping cation with lower valence such as Sr^{2+} into La_2WO_6., the non-stoichiometry is changed. This could be a kind of way to control the concentration of compensating defects.

$$2MO = 2M_{La}^{/} + V_O^{\bullet\bullet} + 2O_O^X \tag{2-11}$$

When an oxide contains lower valent metal cations, this defect is considered as negative effective charge $Sr_{La}^{/}$. This has to be compensated by defects with positive effective charge.

This has to be compensated by defects with positive effective charges. The foreign metal atoms are compensated by oxygen vacancies.

If the foreign metal atom has a higher valence, the compensating defects must have negative effective charges.

$$MO_2 = M_{La}^{\bullet} + \frac{3}{2}O_O^X + e' + \frac{1}{4}O_2(g) \tag{2-12}$$

If the compensating defects are electronic, the dopant may determine the type of conductivity in the oxide, p-type conductivity of n-type conductivity.

2.4 Defect structures of La_2WO_6

The description of the point and electronic defects in a compound and their concentration as a function of the activities of the constituents (or partial pressures, when gases are introduced into the system) and the temperature is the defect structure.

In order to investigate electrical properties, it is common to plot the variation of defect concentrations vs. log pO_2 or vs. log pH_2O. This kind of plots are often referred to Brouwer diagrams which are used to illustrate schematically the behavior of defect concentrations under simplified limiting cases of dominating defects.

2.4.1Defect concentrations as a function of pO_2

Defect reactions:

$$2v_O^{\bullet\bullet} + O_2 = 2O_O^X + 4h^{\bullet} \tag{2-13}$$

$$\mathrm{K_{vo}} = \exp(\frac{\Delta S_{vo}}{R})\exp(\frac{-\Delta H_{vo}}{RT}) = \frac{[O_O^X]^2 p^4}{[v_O^{\bullet\bullet}]p_{O2}} \tag{2-14}$$

$$2[v_O^{\bullet\bullet}] + p = [A'] = cons\tan t \tag{2-15}$$

$$O_2 = 2O_i'' + 4h^{\bullet} \tag{2-16}$$

$$\mathrm{K_i} = \exp(\frac{\Delta S}{R})\exp(\frac{-\Delta H}{RT}) = \frac{[O_i'']^2 p^4}{p_{O2}} \tag{2-17}$$

$$p = [A^{/}] + 2[O_i^{//}] \tag{2-18}$$

$$\sigma_{vo} = \sigma_{vo}^{0} T^{-1} \exp(-\frac{E_a}{kT}) = z_{vo} e c_{vo} \mu_{vo}^{0} T^{-1} \exp(-\frac{E_a}{kT}) \tag{2-19}$$

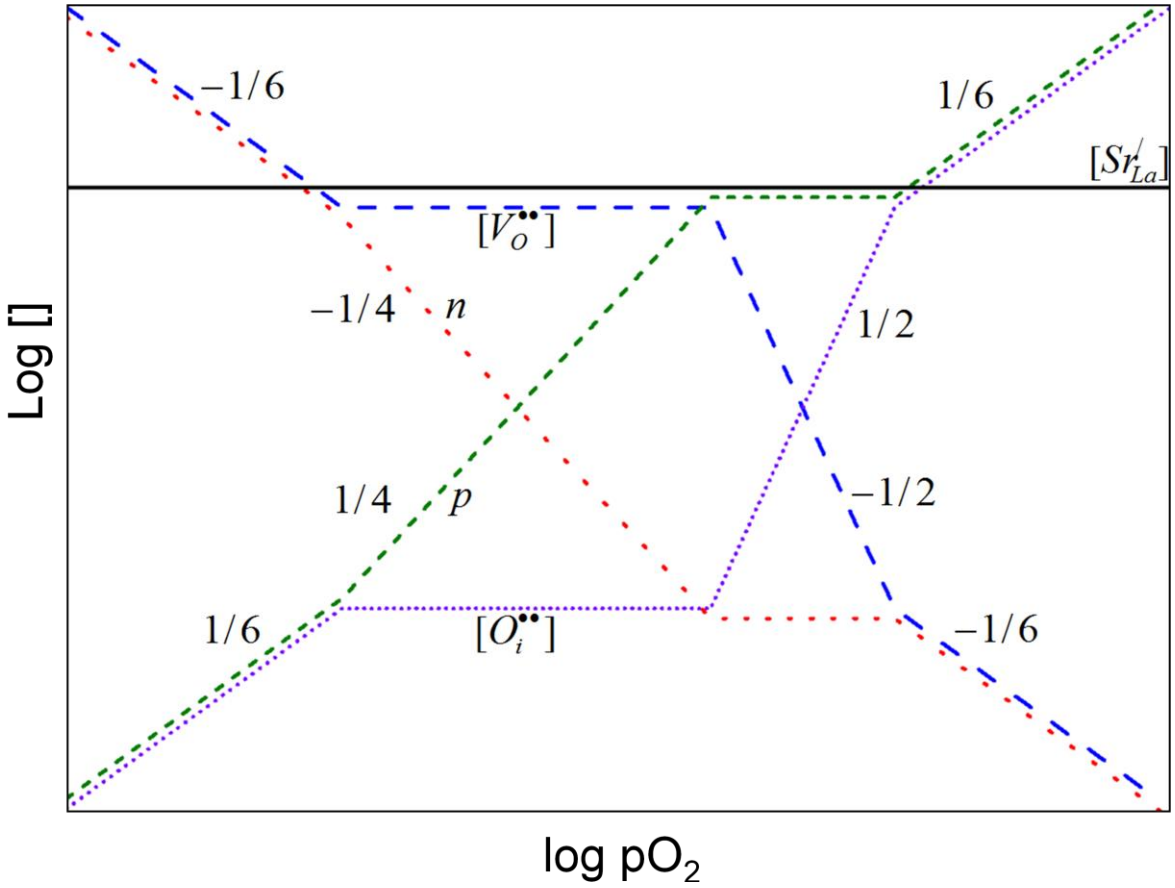

Fig. 2-1 Brouwer diagram of defect concentration vs. p (O2) at constant T for for acceptor doped La_2WO_6

2.4.2 Defect concentrations as a function of pH_2O

$$H_2O(g) + v_O^{\bullet\bullet} + O_O^X = 2OH_O^{\bullet} \tag{2-20}$$

$$K_H = \exp(\frac{\Delta S_H}{R}) \exp(\frac{-\Delta H_H}{RT}) = \frac{[OH_O^{\bullet}]^2}{[v_O^{\bullet\bullet}][O_O^X] p_{H_2O}} \tag{2-21}$$

$$2[v_O^{\bullet\bullet}] + [OH_O^{\bullet}] = [A^{/}] \tag{2-22}$$

$$\sigma_{total} = \sigma_{v_O^{\bullet\bullet}} + \sigma_{H^{\bullet}} \tag{2-23}$$

$$\sigma_{H^\bullet} = \sigma_H^0 . T^{-1} \exp(-\frac{E_a}{kT}) = z_H . ec_H . \mu_H^0 . T^{-1} \exp(-\frac{E_a}{kT}) \quad (2\text{-}24)$$

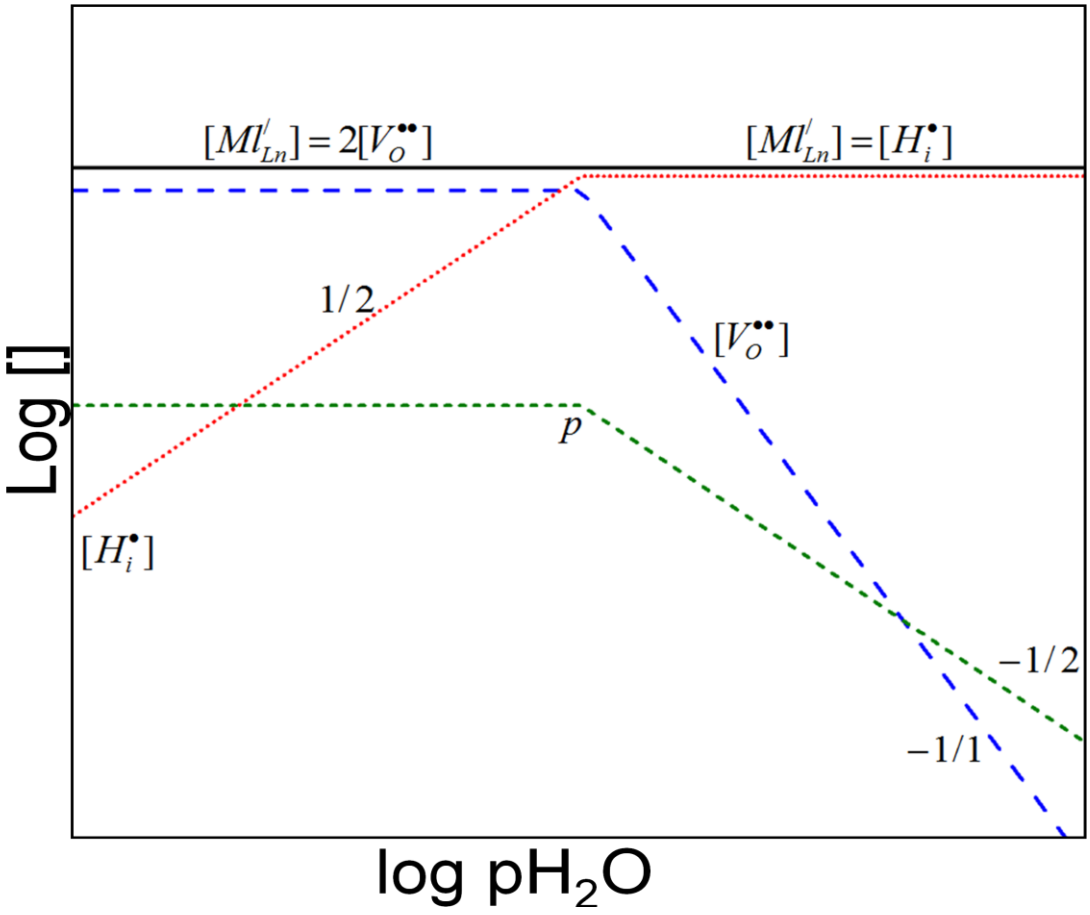

Fig. 2-1 Brouwer diagram of defect concentration vs. p (H_2O) at constant T and p (O_2) for acceptor doped La_2WO_6

2.5 Diffusion

2.5.1 Fick's First law

Fick's laws are the basis for the equations derived in this section. The first law states that the flux of the diffusing species i is proportional to the concentration gradient.

$$J_i = -D_i \left(\frac{\partial c_i}{\partial x} \right)_t \quad (2\text{-}25)$$

J_i is the flux and $\partial c_i / \partial x$ is the concentration gradient. It is assumed that the diffusion coefficient D is constant and independent of the concentration gradient, and that the concentration gradient does not vary with time.

In many systems it is more common that the concentration gradient varies with time. In this case Fick's second law is used.

$$\frac{\partial c_i}{\partial t} = \frac{\partial}{\partial x}\left(D_i \frac{\partial c_i}{\partial x} \right) \tag{2-26}$$

This equation may be solved analytically if the boundary conditions are specified.

The relation between the diffusion coefficient and mobility is given by the Nernst-Einstein relation:

$$\mu_i = D_i \frac{z_i e}{kT} \tag{2-27}$$

2.5.2 Diffusion mechanisms

There are several ways for diffusion for ions in solid crystals as shown below

Vacancy mechanism

If the atoms move in the direction opposite the vacancies, the diffusion occurs by a vacancy mechanism.

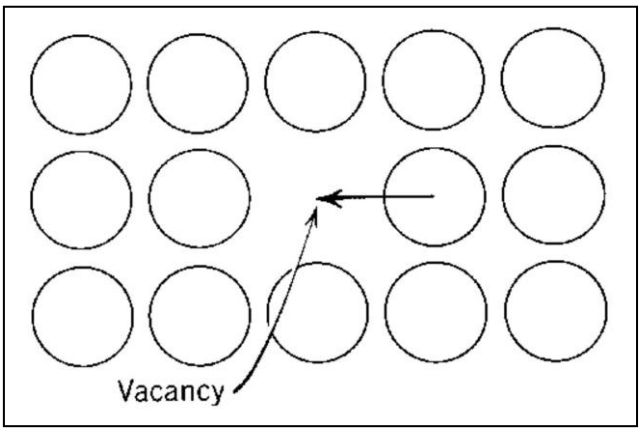

Fig.2-3 Schematic illustration of vacancy diffusion in solids [8]

Interstitial mechanism

If an atom on an interstitial site moves to one of the neighboring interstitial sites, the diffusion occurs by an interstitial mechanism.

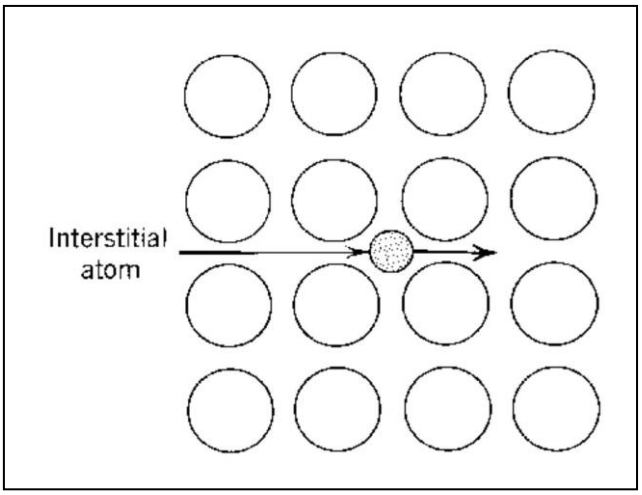

Fig.2-4 Schematic illustration of interstitial diffusion in solids [8]

Interstitialcy mechanism

If the atom on the normal site is pushing in the same direction as that of the interstitial atom, the jump is termed collinear. If the atom is pushed to one of the other neighbouring sites and the jump direction is different from that of the interstitial atom, the jump is termed non-linear.

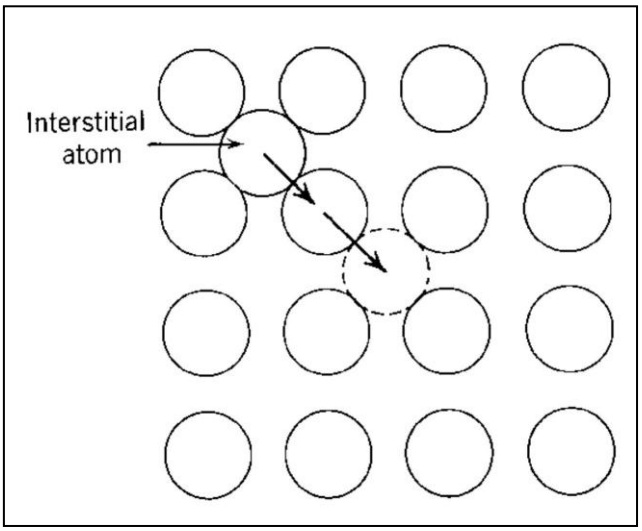

Fig.2-5 Schematic illustration of interstitialcy diffusion in solids, collinear jump [8]

Proton diffusion mechanism

In principle the protons may move by two different mechanisms: i) Grotthuss mechanism or ii) vehicle mechanism.

Grotthuss mechanism: Protons jump from one oxide ion to a neighboring one. After each jump, the proton in the hydroxide rotates, and the proton reorients in the electron cloud and becomes aligned for the next jump. The rotation and reorientation is believed to involve small activation energy and the jump itself is considered to be the rate determining step.

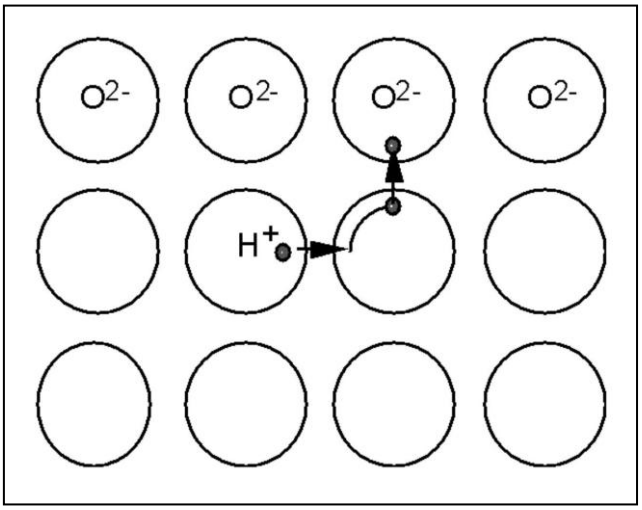

Fig 2-6. Schematic illustration of free transport of protons in metal oxides (Grotthuss mechanism)[8]

Vehicle mechanism: proton is transported as a passenger on an oxide ion, or to be considered as a constitute transport of hydroxide ion. The activation energy for jumping is smaller than that of the oxygen ion due to the smaller raius and charge.

2.6 Charge mobilities of proton and electron

The temperature dependence of the charge carrier mobility is dependent on the electronic structure of the solid. Therefore, the mobility dependency on temperature is divided into non-polar and polar oxides terms.

For a pure non-polar semiconductor the electrons in the conduction band and the electron holes in the valence band can be considered as quasi-free particles. In one case the lattice vibrations result in electron and hole scattering and the mobilities of electrons and holes are determined by the thermal vibrations of the lattice. Another case is that, the scattering is

mainly due to irregularities caused by impurities or other imperfections, the two scattering mechanisms have different temperature dependencies, as follows:

$$\mu_{n,latt} = \mu_{n,latt,0} \times T^{-3/2} \tag{2-28}$$

$$\mu_{n,imp} = \mu_{n,imp,0} \times T^{-3/2} \tag{2-29}$$

The mobility is given by

$$\mu = \frac{1}{\frac{1}{\mu_{latt}} + \frac{1}{\mu_{imp}}} \tag{2-30}$$

In ionic oxies, the electrons and electron holes move through and polarize the neighboring lattice and cause a local deformation of the structure. This forms polaron which could be considered as a single particle. For highly ionic non-transition metal oxides, the large polar mechanism is suggested given by

$$\mu_{l\arg epol.} = \mu_{l\arg epol.0} \times T^{-1/2} \tag{2-31}$$

For other oxides, the small polaron mechanism is suggested. The mobility of a small polaron can be described by classical diffusion mechanism. Nernst-Einstein equation can be used to relate the activation energy of jumping at high temperatures. The temperature dependency of the mobility for a small polaron is given by

$$\mu = \mu_{l0} T^{-1} \exp(-\frac{E_u}{kT}) \tag{2-32}$$

Where E_u is the activation energy for jumping. This equation could be used for describing mobility dependency on temperature for electrons, electron holes and as well as protons. In evaluating the activation energy associated with the diffusion coefficient from conductivity measurements, it is necessary to plot log ($\sigma_i T$) vs. 1/T

2.7 Eletrical conductivity

The driving force of diffusion in metal oxides is given by the negative potential gradient. The expression following gives the force exerted on a charged particle of type i with charge $z_i e$:

$$F = -zie\frac{d\phi}{dx} = zieE \tag{2-33}$$

Where ϕ is the electrical potential and $E = -\frac{d\phi}{dx}$ is the electric field. The current density i_i is given by the product of flux and charge:

$$i_i = z_i e j_i = z_i e c_i B_i F = (z_i e) 2B_i \, c_i E = z_i e c_i \mu_i E = \sigma_i E \tag{2-34}$$

Where B_i is the mechanical mobility of the particle, the charge mobility μ_i is the charge $z_i e$ times B_i on each particle and σ_i is the electrical conductivity of the charge species i.

$$\sigma_{total} = \Sigma\sigma_i \tag{2-35}$$

The total conductivity should be equal to the sum of partial conductivity. The ratio of the partial conductivity σ_i to the total conductivity is termed the transport number of species i:

$$t_i = \frac{\sigma_i}{\sigma_{total}} \tag{2-36}$$

2.8 Isotope effect

In free migration of proton, isotope effects are more important than other diffusion processes, due to the unique 1:2:3 mass ratios of the protium (H), deuterium (D), and tritium (T) isotopes of hydrogen. One of the effects are recognized[9]:

(1) The “classical” difference: The preexponential of diffusion is inversely proportional to the square root of the mass of the hydrogen isotope: $D_H : D_D : D_T = 1 : (1/\sqrt{2}) : (1/\sqrt{3})$

These substantial ratios are available to detect, they are often used to distinguish free hydrogen migration and vehicle mechanisms.

(2) The “non-classical” difference: Hydrogen isotopes have different zero-point energy levels due to their different masses which gives rise to a difference in the activation energy for deuterium diffusion is theoretically around 0.55ev (5.7kJ/mol) higher than for protium diffusion.

(3) Tunneling: The proton atom and proton is a particle which is light enough to make tunneling possible. The effect is normally to enhance hydrogen diffusion at low temperatures,

compared to the extrapolation of the high-temperature Arrhenius expression. The isotope effect here arises because tunneling is of comparatively little importance for deuterium and tritium as their masses are too high.

2.9 Electrochemical impedance spectroscopy (EIS)

Electrochemical impedance spectroscopy (EIS) is a very powerful method for characterizing many of the electrical properties of materials and their interfaces, and it can be used to investigate the dynamics of bound or mobile charge in the bulk or interfacial regions in solids as well as liquids: semiconductors, ionic conductors and even insulators[10].

In practical applications, EIS could be used for measuring conductivity in ionically conducting solids, the characteristic response of each region present in the electromaterial, e.g. grain boundary and bulk regions, and will allow extracting their conductivity and capacitance values.

EIS is based on applying a sinusoidal voltage of variable frequency and very small amplitude over the sample. The current through the electrolyte should remain small, in order to avoid polarization problems and/or irreversibly damage the material.

For metals and semiconductors, the conductivity could be obtained from resistance measurements if the geometric factors are given. When a voltage bias is applied, current will flow through the material. The resistance could then be calculated using Ohm's law:

$$R = \frac{V}{I} \tag{2-37}$$

Where $R = \frac{d}{A\sigma}$ (2-38)

Where R, V, I, d, A and σ are the resistance, applied voltage, measured current, sample thickness, surface area, and conductivity.

However, in an ionic or mixed conductor, Ohm's law is not valid. When a voltage difference is applied to an ionic conductor, ions or ion vacancies move to one of the electrodes (positively charged ions/vacancies will move to the negative electrode and vice versa). This movement causes a polarization of the material due to the accumulation of charges at the electrodes. Such a polarization causes current drops with variation of time

Impedance may be defined as the opposition to charge flow in a system, given by:

$$Z^* = \frac{V}{I} \tag{2-39}$$

Z* is a complex number, which may be expressed as

$$Z^* = Z' - j\frac{V}{I} \tag{2-40}$$

with $j^2 = -1$. The real part of the impedance, $Z^{|}$, comprises the resistive component, R, whilst the imaginary part, $Z^{||}$, includes capacitive and inductive components. Impedance data can be presented in a complex plane representation, $Z^{|}$ against $Z^{||}$. An alternative representation can be used in which $Z^{||}$ or $Z^{|}$ are plotted against frequency. The admittance is defined as the inverse of the impedance, $Y^* = (Z^*)^{-1}$, and denotes the each of charge flow through the system. In a heterogeneous system, impedance and admittance plots emphasize those elements which have the largest resistances.

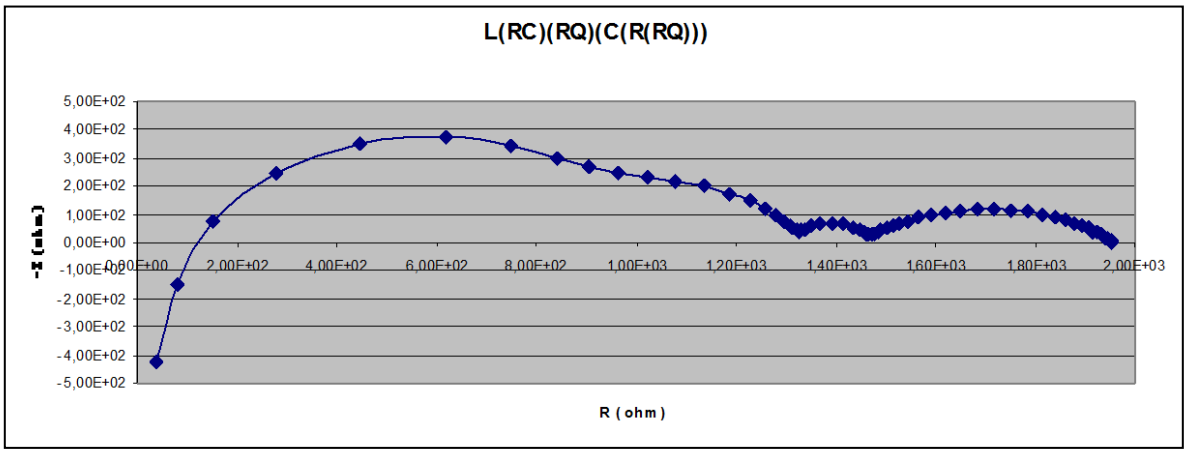

Fig. 2-3 Nyquist impedance plot for a typical ceramic sample[11]

Frequently, the experimental data for many systems give complex plane diagrams that form circular arcs with centers lying below the axis (that is a depressed semicircle). This is the so-called dispersing phenomenon. In the case of the dispersing effect, the double-layer capacitance and pseudo-capacitance involved in electrochemical reactions do not function as pure capacitors, but as constant phase elements (CPEs), whose admittance and impedance, respectively, are defined as:

$$Y_{CPE} = Y_0 (j\omega)\alpha \tag{2-41}$$

And

$$Z_{CPE} = 1/Y_0(j\omega)\alpha \tag{2-42}$$

Where Y_0 is the admittance magnitude and α the exponential term; α = 1 in a perfect capacitor and α = 0 for a pure resistor. Capacitors should be substituted for CPEs in the equivalent circuits to result in a better fit when the dispersing impedance data are encountered.

Table 3-1 Capacitance values and their conventional interpretation[12]

Capacitance (F)	**Phenomenon responsible**
10^{-12}	Bulk
10^{-11}	Secondary phases
10^{-11} - 10^{-8}	Grain boundary
10^{-10} - 10^{-9}	Bulk, ferroelectric
10^{-9} - 10^{-7}	Surface layer
10^{-7} - 10^{-}5	Sample electrode interphase
10^{-4}	Electrochemical reactions

3. Literatures

Protonic conduction at elevated temperature has been reported in several solid materials[13]. In the early 1980s, materials based on perovskite-type oxides, such as acceptor doped $SrCeO_3$ and $CaZrO_3$, exhibited protonic conduction under wet conditions at high temperatures. Materials based on rare earth oxoacid salts, such as phosphates[14, 15], borates [16], silicates [17] and rare-earth ortho-niobates and ortho-tantalates [18] were also reported as protonic conductors with high chemical stability. These are the main types of solid proton conducting materials found up to now, but proton conduction is not restricted to these classes of materials.

The existence of proton conductivity in La_6WO_{12} was firstly reported by Shimura et al.[19]. The effects of doping were also investigated [2], and it was reported that La_6WO_{12} (the stoichiometry was modified as $La_{5.3\text{-}5.7}WO_{12\text{-}\delta}$ [5]) based materials could reach proton conductivities in the order of 3×10^{-03} S/cm at approximately 800°C[2, 4]. Lately, investigations on Gd_6WO_{12} [20] and Er_6WO_{12} [4]were also carried out, both of which showed interesting electrical transport properties as well.

3.1 Ln_6WO_{12} (Ln=La, Nd, Gd, Er)

3.1.1 Electrical properties of Ln_6WO_{12} (Ln=La, Nd, Gd, Er)

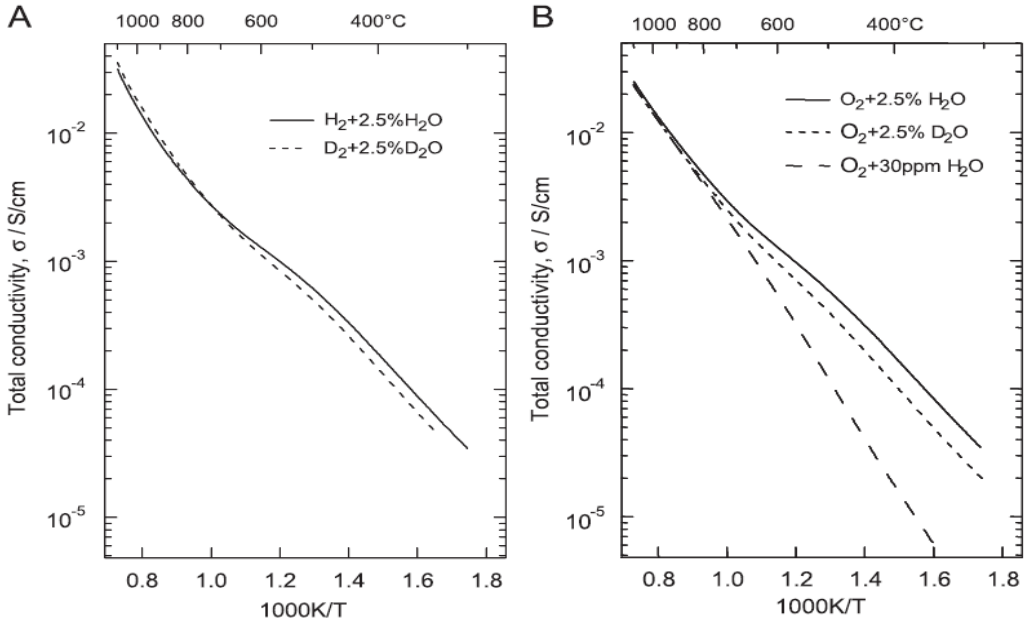

Fig.3-1 Total conductivity as a function of the inverse absolute temperature for LaW1/6O2 in H_2—0.025 H_2O atm and D_2—0.025 D_2O atm (A) and O_2— 0.025 H_2O, O_2 — 0.025 D_2O and O_2 — approximately 3×10^{-5} H_2O atm (B) from 300 to 1100°C[2]

As we can see clearly the isotope effect on conductivity both at reducing and oxidizing conditions, which suggests the existence of proton conductivity.

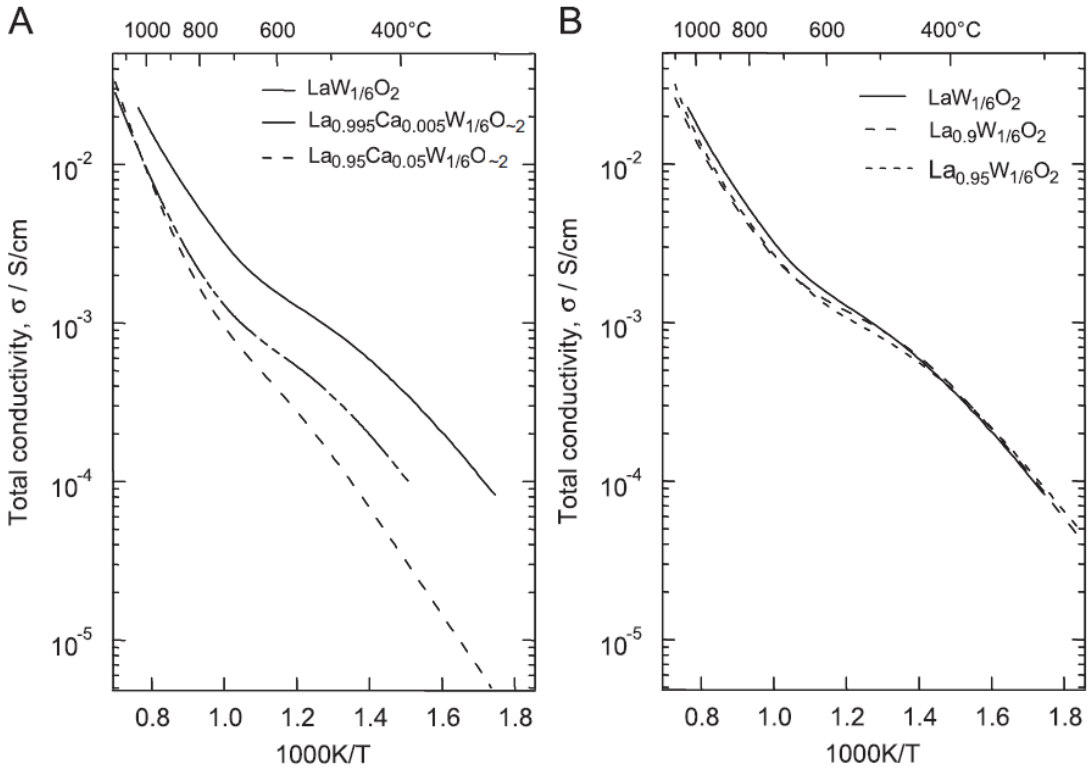

Fig.3-2 Total conductivity as a function of the inverse absolute temperature for $La_{0.95}Ca_{0.05}W_{1/6}O_{\sim2}$, $La_{0.995}Ca_{0.005}W_{1/6}O_{\sim2}$ and $LaW_{1/6}O_2$ (A) and $La_{0.9}W_{1/6}O_2$, $La_{0.95}W_{1/6}O_2$ and $LaW_{1/6}O_2$ (B) as measured in wet hydrogen from 300 to 1100 °C.[2]

From this plot, we could see that pure La_6WO_{12} exhibits higher conductivity than those which were acceptor doped. And also, it could be oberserved that with the increase of doping concentration, the eletrical conductivity decrease.

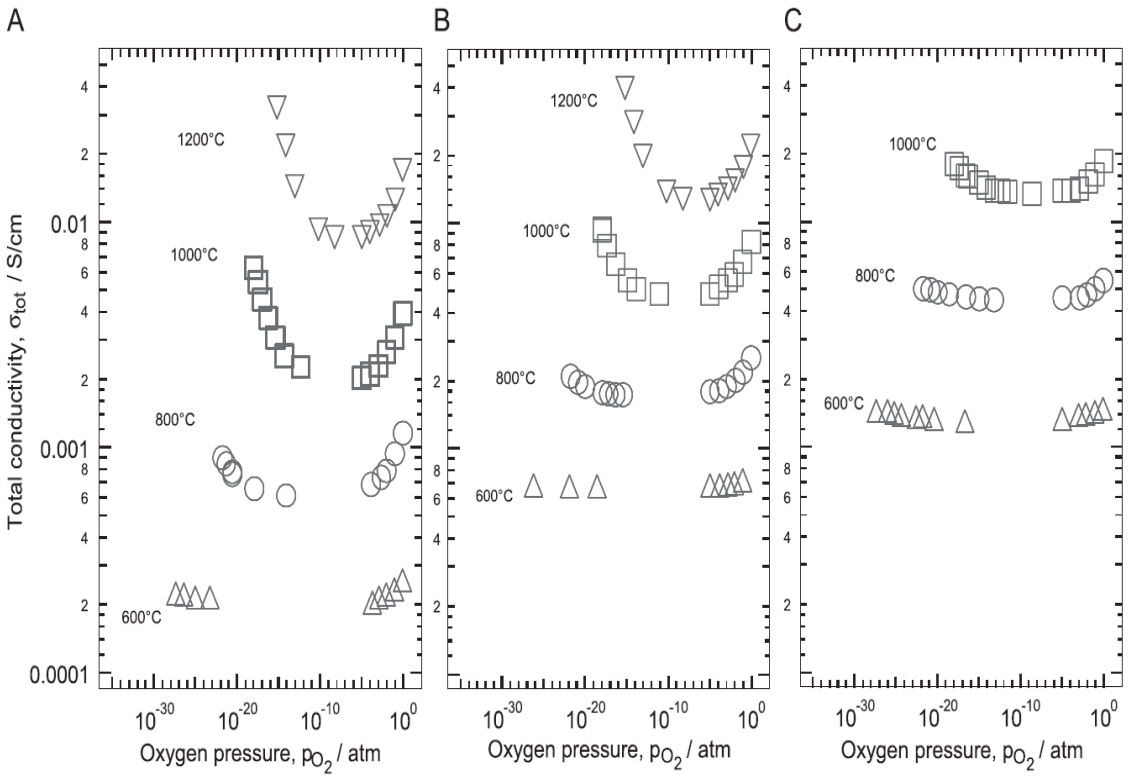

Fig.3-3 Total conductivity as a function of the oxygen partial pressure at different temperatures from 600 to 1200 °C for $La_{0.95}Ca_{0.05}W_{1/6}O_{\sim 2}$ (A),$La_{0.995}Ca_{0.005}W_{1/6}O_{\sim 2}$ (B) and $LaW_{1/6}O_2$ (C). Measurements are performed under wet conditions.[2]

We can see from the plot that conductivity of electronic species(electron and electron hole) as compensating defects exhibits pO_2 dependency both at reducing and oxidizing condition. It is observed that with the increase of dopant concentration, the dependency behavior is more obvious.

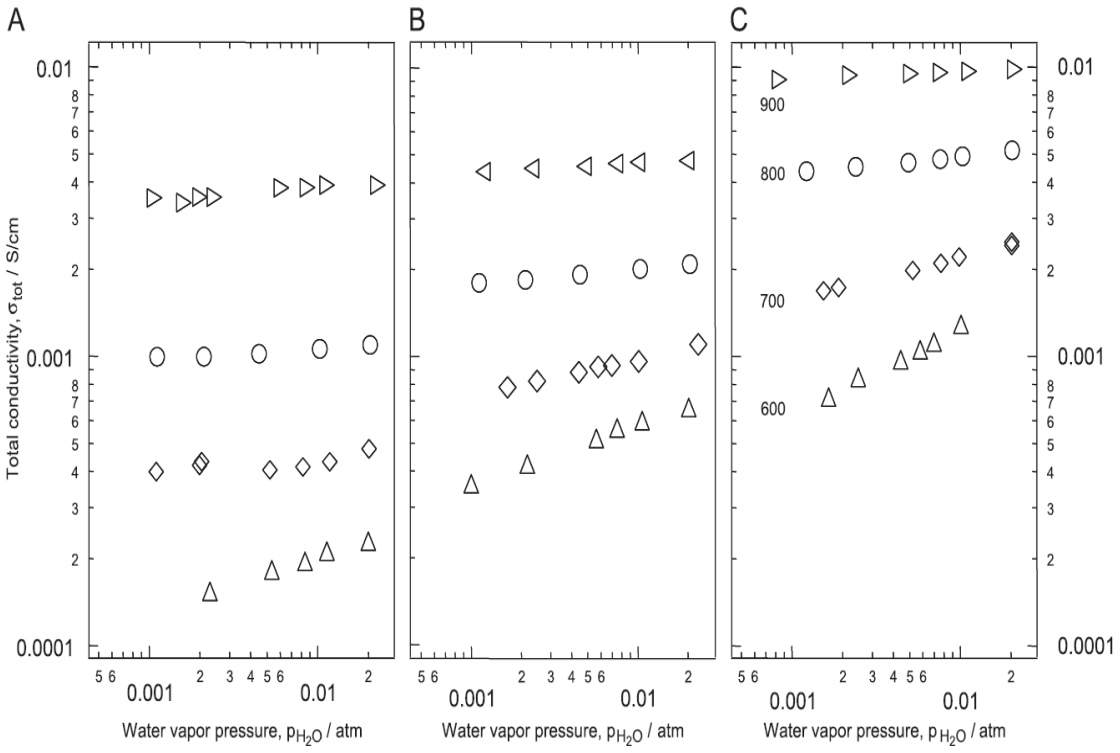

Fig.3-4 Total conductivity as a function of the water vapor partial pressure in hydrogen at different temperatures from 600 to 900°C for $La_{0.95}Ca_{0.05}W_{1/6}O_{\sim 2}$ (A), $La_{0.995}Ca_{0.005}W_{1/6}O_{\sim 2}$ (B) and $LaW_{1/6}O_2$ (C). The oxygen pressure remains essentially constant at each temperature, since the gas mixturesare of constant pH_2O/pH_2 ratio[2]

We can see in O_2 atmosphere, if pH_2O increase, the total conductivity would also increase, the slope for $\log(\sigma_{total})/pH_2O$ decreases when the temperature goes higher, which suggests that when temperature is elevated the proton concentration is decreasing. And also, the dopant concentration have influence on the conductivity as the changes of oxygen vacancy concentration which is regarded have relationship

If we compare the electrical properties of La_6WO_{12} with other Ln_6WO_{12} (Ln=Nd, Gd, Er)

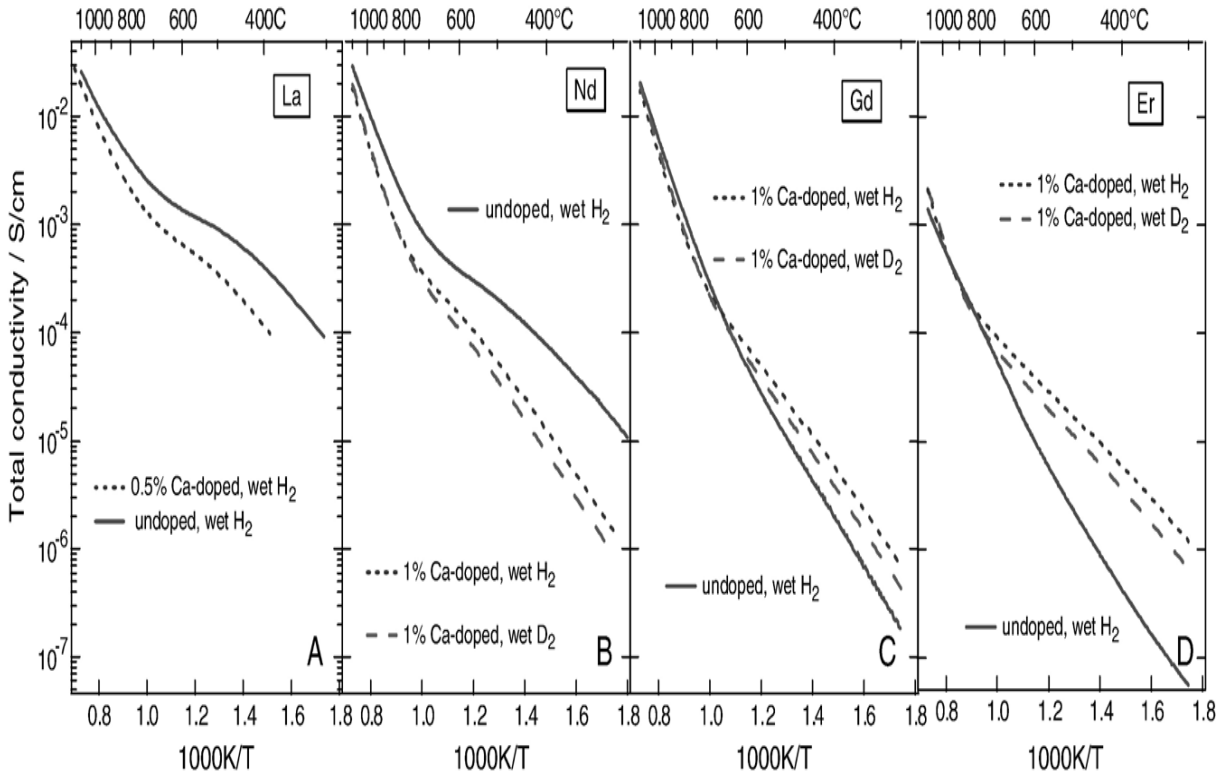

Fig. 3-5 Total ac conductivity (10 kHz) as a function of the 1/T for undoped and Ca-doped, $LnW_{1/6}O_2$, [Ln=La(A), Nd(B), Gd(C), Er(D)] underH_2+2.5% H_2O and D_2+2.5% D_2O atmospheres in the temperature range 300°C to 1100 °C[4]

Each plot shows:

A. The conducitivity decreases when the material is acceptor doped.

B. The conducitivity decreases when the material is acceptor doped. The isotope effect for doped sample which suggests existence of proton conductivity.

C. The conductivity increases when the material is acceptor doped. Also shows isotope effect.

D. The conductivity increases when the material is acceptor doped. Also shows isotope effect.

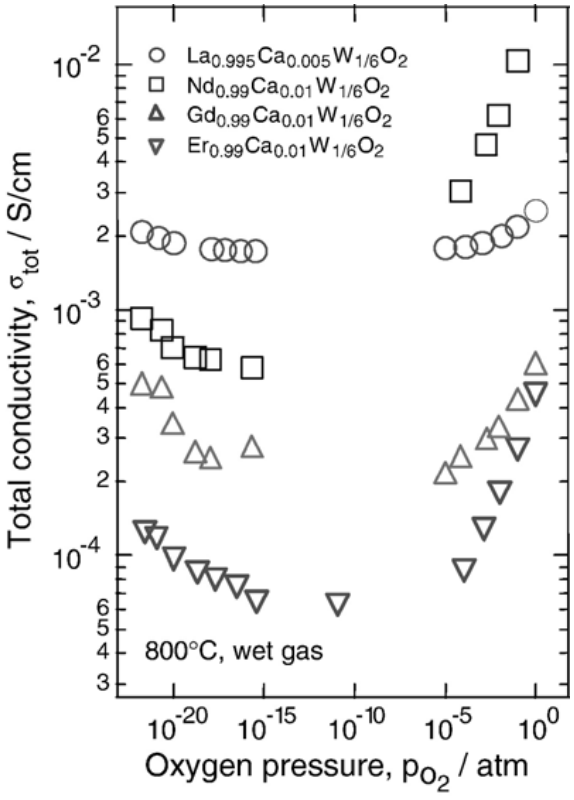

Fig. 3-6. Total ac conductivity (10 kHz) as a function of the oxygen partialpressure for LnW1/6O2 (Ln=La, Nd, Gd, Er) at 800 °C under wetconditions. Left side is acceptor doped[4]

They become electronic semiconductors in oxidizing — and reducing atmospheres at high temperatures.

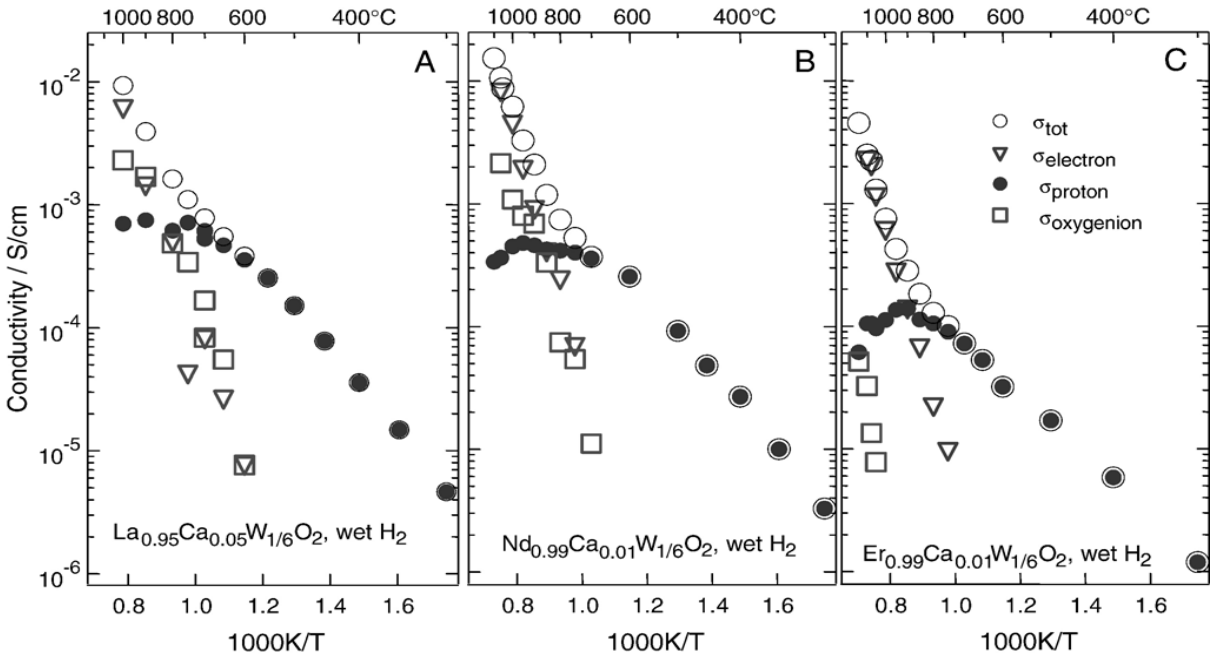

Fig. 3-7 Partial conductivities, as determined from the EMF-technique, as a function of the 1 /T for Ca-doped $LaW_{1/6}O_2$,$NdW_{1/6}O2$ and $ErW_{1/6}O_2$ under H++2.5% H_2O atmospheres in thetemperature range 300 to 1050 °C[4]

A general behavior for the materials is that the conductivity is predominated by protons under wet conditions below approximately 900 °C. Furthermore, they become electronic semiconductors in oxidizing — and reducing atmospheres at high temperatures. The maximum in proton conductivity was observed for nominally undoped $LaW_{1/6}O_2$ with values in the range 3 to 5×10 3 S/cm at approximately 850 °C.

3.1.2 Structures of Ln_6WO_{12} (Ln=La, Nd, Gd, Er)

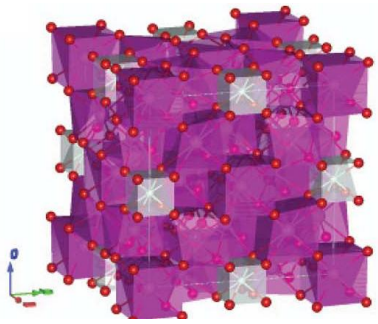

Fig. 3-8 Structure of $La_{5.3\text{-}5.7}WO_{12\text{-}\delta}$ [5]

The structure of $La_{5.3\text{-}5.7}WO_{12\text{-}\delta}$ is cubic, and the formula unit can be written as $La_{6.63}W_{1.17}O_{13.43}$ (Z = 4)[5] While the structures of other Ln_6WO_{12} (Ln= Nd, Gd, Er) are orthorhombic[4].

3.2 RE_2WO_6

3.2.1 La_2WO_6

$RE_XW_YO_Z$ form a group of ceramic materials with numerous stoichiometries as shown in below, whose functional properties are dependent upon the crystalline structure and on the valence of tungsten. Then, a related compound La_2WO_6 is become of interest with which tungsten in valence state +6. The structure of the low-temperature form of β-La_2WO_6 has been determined from laboratory X-ray, neutron time-of-flight and electron diffraction data. The structure consists of octahedral [WO_6] and tetrahedral [OLa_4][7].

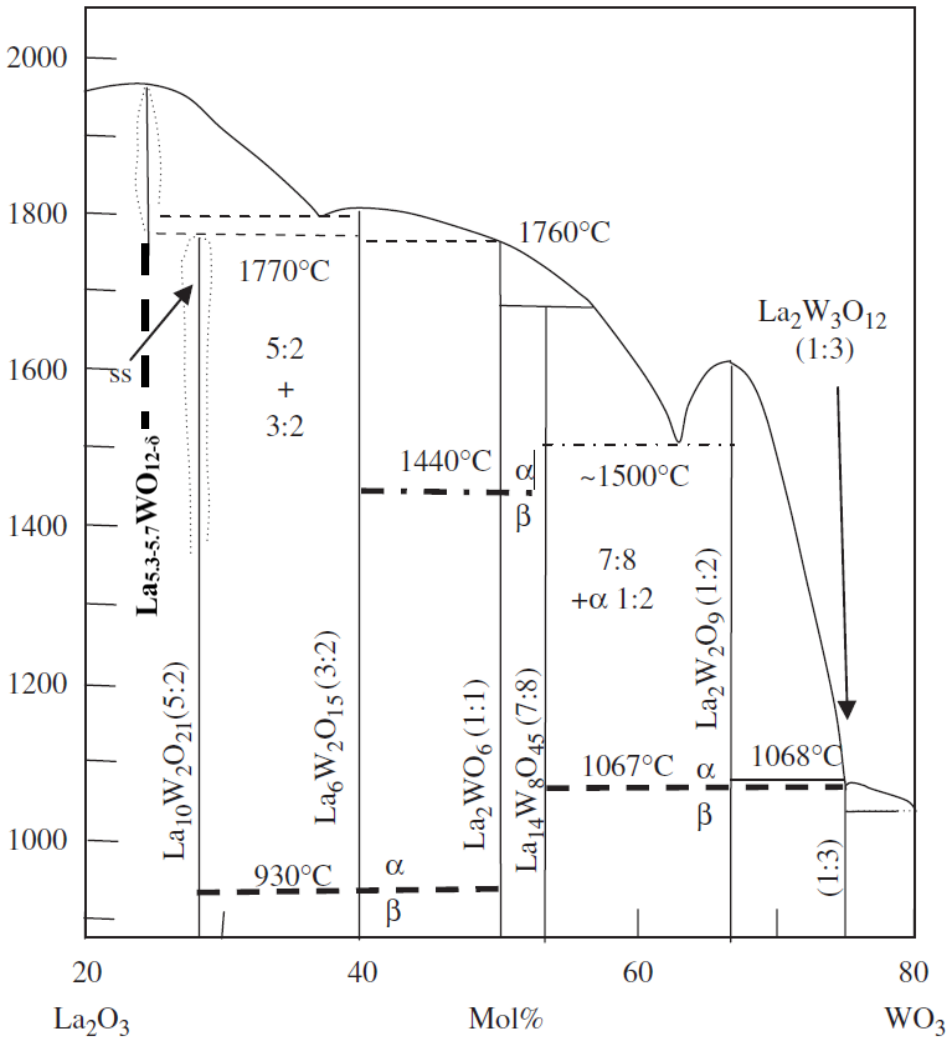

Fig. 3-9 Phase equilibrium diagram for the system La_2O_3-WO_3 [21]

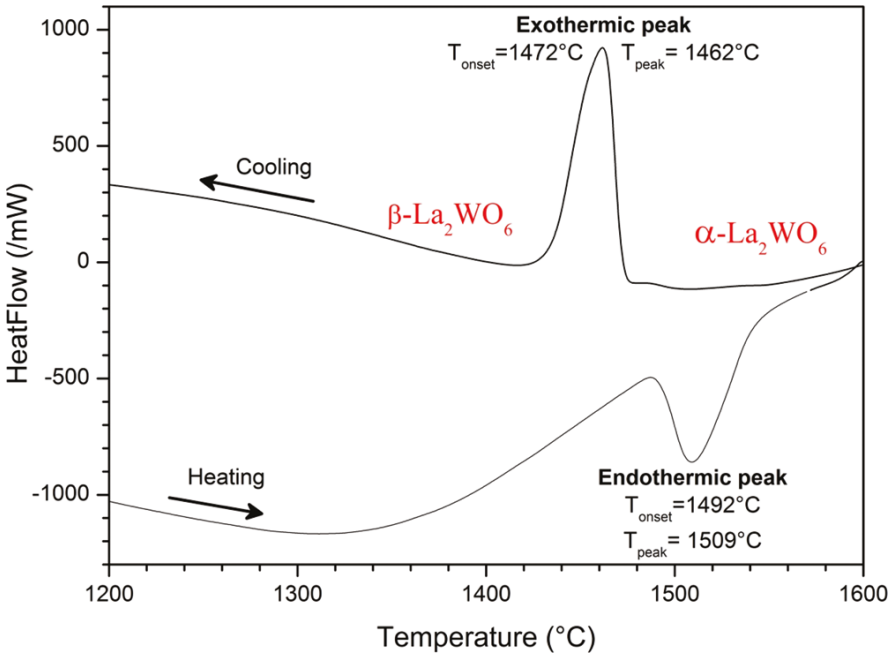

Fig. 3-10 Differential scanning calorimetry analysis for by Mathieu Allix et al.[22]

Mathieu Allix et al. define the transition tempertures for α-La_2WO_6 and β- La_2WO_6.

He also found that α-La_2WO_6 is more conducting than β-La_2WO_6 within 1 order of magnitude (5.5×10^{-4} S/cm at 620 °C)[22].

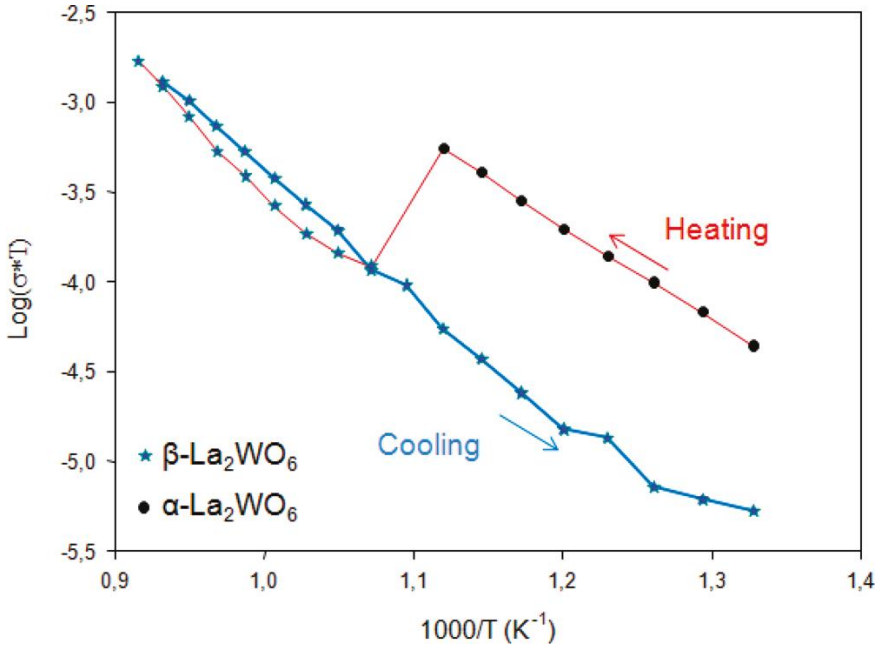

Fig.3-11 Temperature dependence of the electrical conductivity for α-La2WO6 from 640 °C, the plot reports to the α-La_2WO_6 phase [22]

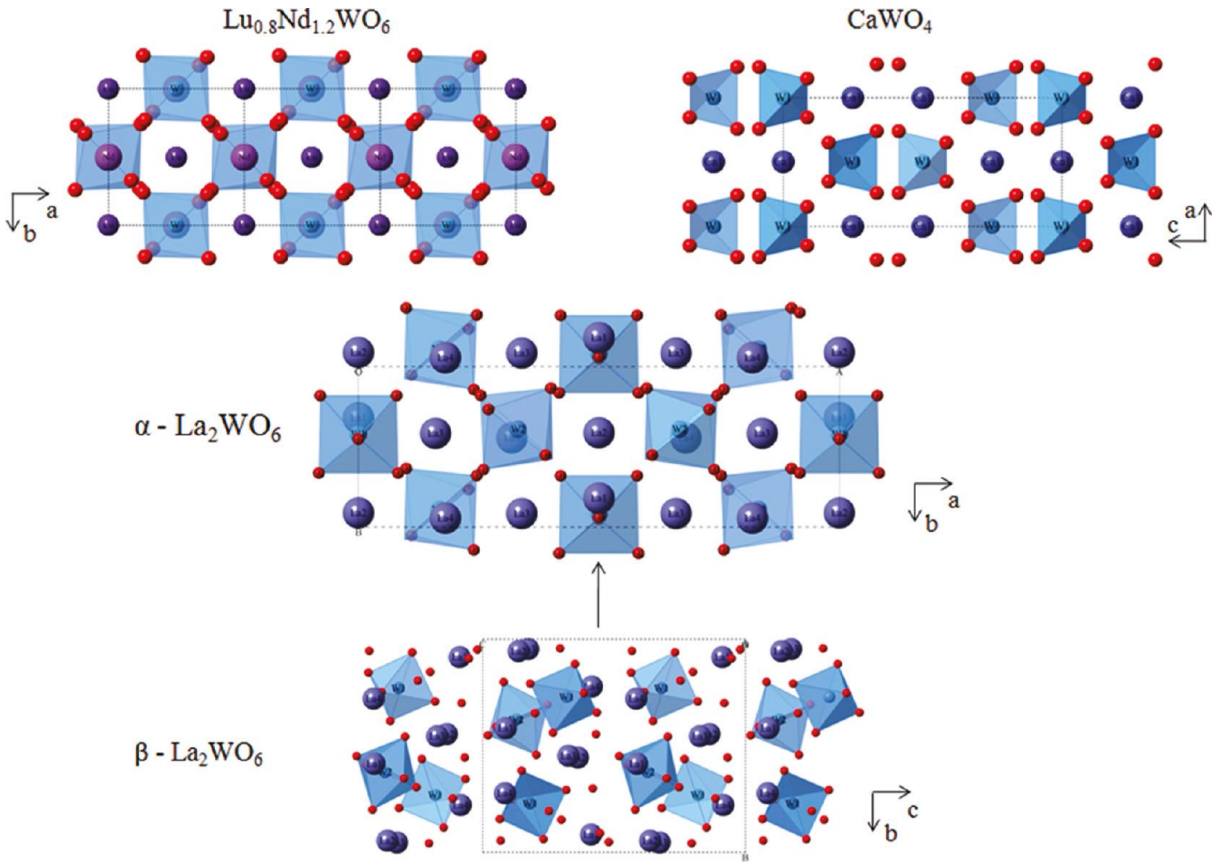

Fig. 3-12 Crystal structures of the β and α-La_2WO_6 phases. They are compared to the $Lu_{0.8}Nd_{1.2}WO_6$ and $CaWO_4$ structures

Then $Lu_{0.8}Nd_{1.2}WO_6$ is also become of interest.

4. Experimental

4.1 Sample preparation

In this work, samples of acceptor doped La_2WO_6 were synthesized both in solid state and wet chemical synthesis method. Samples of $Nd_{1.2}Lu_{0.8}WO_6$ with different dopants were synthesized in wet chemical method.

In order to obtain pure β-$La_{1.96}Sr_{0.04}WO_{6-\delta}$, sample 1 and 2 were obtained in solid state synthesis method and wet chemical synthesis separately. Since sample 3 and 4 has more complex composition, they were obtained in wet chemical synthesis method, which could provide better mix of the precursors.

Sample 1: β-$La_{1.96}Sr_{0.04}WO_{6-\delta}$ obtained by solid state synthesis method

La_2O_3 was preheated at 1000°C for 1 hour in a furnace to remove the crystallization water, and taken out from the furnace at 600°C and cooled in a desiccators with alumina plate. $SrCO_3$ and WO_3 were preheated at 250°C for half a hour. Stochiometric proportions of La_2O_3, $SrCO_3$ and WO_3 were mixed and ground together, made into a pellet and heated to 1400°C for 12 hrs[7]. A dense grayish dense pellet was obtained. Discolor was observed on the surface of sample 1.

Sample 2: β-$La_{1.96}Sr_{0.04}WO_{6-\delta}$ obtained by wet chemical synthesis method

La_2O_3 was preheated at 1000°C for 1 hour in a furnace to remove the crystallization water, and taken out from the furnace at 600°C and cooled in desiccators with alumina plate. $SrCO_3$ and WO_3 were preheated at 250°C for half a hour. Stochiometric proportions of La_2O_3, $SrCO_3$ and WO_3 were dissolved HNO_3 solution and $NH_4{\cdot}OH$ solution, each solution was added with EDTA as the chelating complex agent, the solutions were neutralized with pH value 7-8 and mixed without visible precipitation[5]. The mixed solution was heated to 300 °C on a hot plate with stirring. A gel was formed rapidly and transferred into a heat cabin heat up to 225 °C. White and fluffy power was obtained. After de-carbonization at 600°C for four hours, the fluffy powers was ground in order to decrease the fissures between the particles, and made into a pellet and sintered at 1200°C for 5.5 hrs. As there is possibility that WO_3 would evaporate during sintering process, the pellet was coated by the some extra β-$La_{1.96}Sr_{0.04}WO_{6-\delta}$ powder. After sintering stage, a grayish dense ceramic pellet was obtained after removing the porous β-$La_{1.96}Sr_{0.04}WO_{6-\delta}$ coating, no discolor was observed on the surfaces.

Sample 3: $Nd_{1.176}Ca_{0.024}Lu_{1.176}Mg_{0.04}WO_{6-\delta}$ was obtained by wet chemical synthesis

Nd_2O_3, Lu_2O_3, $CaCO_3$, $Mg(OH)_2$ and WO_3 were pre-heated separately. Stoichiometric proportions of Nd_2O_3, $SrCO_3$ and WO_3 were dissolved HNO_3 solution and $NH_4{\cdot}OH$ solution, EDTA was used as the chelating complex agent, after adjusting the pH value and water evaporation as the synthesis of sample 2. The combustion temperature was 263 °C. Blue and fluffy power was obtained. After de-carbonization and grinding, the powder was made into a pellet and heated up to 1500°C for 5.5 hrs. A ceramic pellet was obtained. (The sample appears purple in sunlight and blue in artificial lights.

Sample 4: $Nd_{1.176}Ca_{0.04}Lu_{1.176}WO_{6-\delta}$ was obtained by wet chemical synthesis

The synthesis process of sample 4 was the similar to that of sample 3 but with different stoichiometric of starting materials.

4.2 Structural and microstructural characterization

4.2.1 Powder XRD

Working principle: crystals consists of planes of atoms that are spaced a distance d, but can be resolved into many atomic planes, each with a different d-spacing. A, b and c (length) and α, β and γ (angles) between a, b and c are lattice constants which can be determined by X-Ray Diffraction (XRD).

Diffraction occurs only when Bragg's law is satisfied (condition for constructive interference from planes with spacing d):

$$D = \frac{n\lambda}{2 \bullet \sin\theta} \tag{4-1}$$

The variable d is the distance between atomic layers in a crystal, and the variable lambda λ is the wavelength of the incident X-ray beam; n is an integer.

X-ray crystallography is a standard technique for solving crystal structures. Its basic theory was developed soon after X-rays were first discovered more than a century ago, and still today, X-Ray crystallography is widely used in materials and biological research. The continual development is data collection instrumentation and data reduction methods have been a great improvement. The advent of synchrotron radiation sources, area decor based data collection instruments, and high speed computers has dramatically enhanced the efficiency of crystallographic structural determination. Powder XRD is perhaps the most widely used X-Ray diffraction technique for characterizing materials. As the name suggests, the sample is usually in a powdery form. The detection limit of the technique is 1-3%.

Powder diffraction data can be collected using either transmission or reflection geometry. As the particles in the power sample are randomly oriented, these two methods will yield the same data.

In this work, powder XRD patterns for the sintered pellets at room temperature were collected with a Bruker D8 Apex 3-circle diffractometer, Mo Kα radiation from a sealed tube (no optics). Apex CCD area detector. The scans were performed in the 2θ range (10°-90°) for 10 times.

4.2.2 SEM

Working principle: SEM has three-dimensional appearance and is useful for judging the surface structure of a sample. In a typical SEM, electrons are emitted from a tungsten or lanthanum hexaboride (LaB_6) cathode and are accelerated towards an anode; alternatively, electrons can be emitted via field emission $(FE)^n$, which has a higher resolution. The most common imaging mode monitors low energy (<50 eV) secondary electrons (SE), which results in images with a well-defined, three-dimensional appearance. In addition to the secondary electrons, backscattered electrons (BSE) can also be detected. BSE may be used to detect contrast between areas with different chemical compositions. These can be observed especially when the average atomic number of the various regions is significantly different.

In this work, the microstructure of the sintered pellets was observed with a Scanning Electron Microscope (Quanta 200 FEG, FEI).

4.3 Experimental set up for electrical measurements

4.3.1 Schematic illustration of the appratus

The set-up for measuring electrical conductivity of ceramic samples is illustrated in Fig 4-1.

The sample was placed in a measurement cell, which is connected to a PID controller for temperature monitoring and controlling, to a gas-mixing system through gas lines for measurement cell atmosphere control and to impedance devices for electrical measurements. When cell is heated to elevated temperatures, cooling water is used.

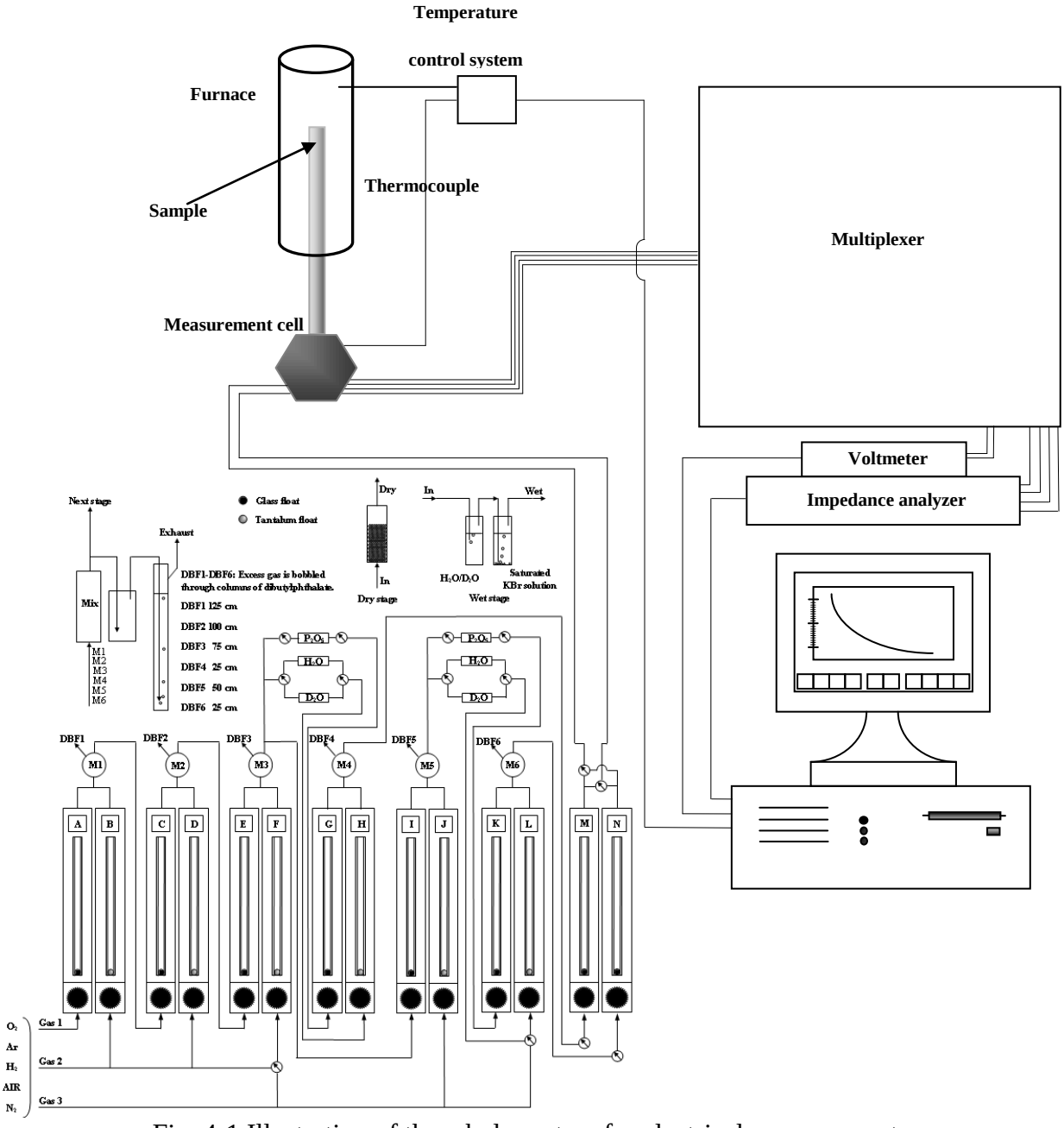

Fig. 4-1 Illustration of the whole system for electrical measurement

4.3.2 Measurement cell

The ceramic samples are placed in a ProboStat^{TM} cell as a measurement cell as illustrated below in fig. 4-2

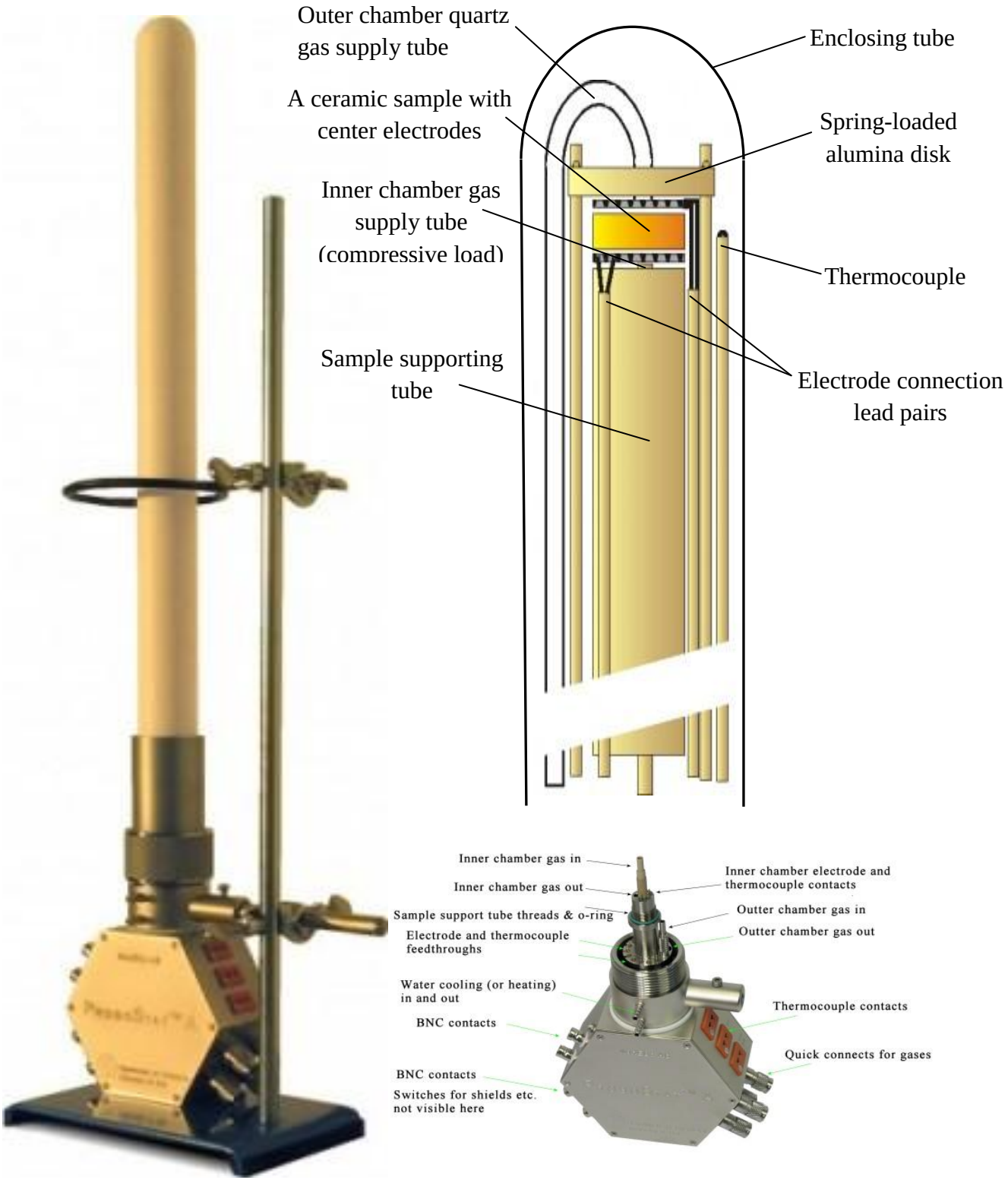

Fig. 4-2 Illustration of a ProboStat^{TM} cell[23]

The measuring cell has two chambers which are separated by the sample placed on the supporting tube. The sample with cater Pt electrodes is pressed onto the tube by a spring loaded alumina disk. The partial pressures of different gas mixtures could be controlled by the gas-mixing unit. The chamber is equipped with a thermocouple.

4.3.3 Temperature control device

The temperature of the measurement call was monitored and controlled by a PID regulator (Eurotherm 2216e), the measurement cell is connected to the PID controller with a thermocouple.

4.3.4 Impedance measuring devices

The conductance of the samples was measured with the Solartron 1260 and HP 4192A impedance analyzer with an ac frequency of 10 kHz and an oscillation voltage of 0.5V. Impedance sweep at specific temperature and temperature was measured at deviating frequencies ranging from 1Hz to 1MHz in order to distinguish the contribution from bulk, grain boundaries and electrodes.

The total conductivity of the samples was obtained by taking the thickness, electrode area of the sample and relative density into account.

$$\sigma_{sepcific} = G_{measured} \frac{\mathrm{d}}{A} \frac{1}{(RD)^2} \tag{4-2}$$

d: thickness

A: electrode area

RD: relative density of the sample, calculated by

$$RD = \frac{\rho_{sample}}{\rho_{reference}} \tag{4-3}$$

The pellets dimensions were determined by a venires caliper, the mass were determined by electronic balance. The relative densities of the ceramic pellets were calculated by the actual density divided by the calculated density.

The term contact resistance refers to the contribution to the total resistance of a material, which comes form the electrical leads and connections as opposed to the intrinsic resistance,

4.3.5 Gas-mixing system

The function of the gas-mixing system to provide possibilities for mixing different gas in various ratios in order to control the partial pressures of different gas in the gas mixture. The schematic drawing of the gas-mixing system with six mixing stages is illustrated below as fig.4-3

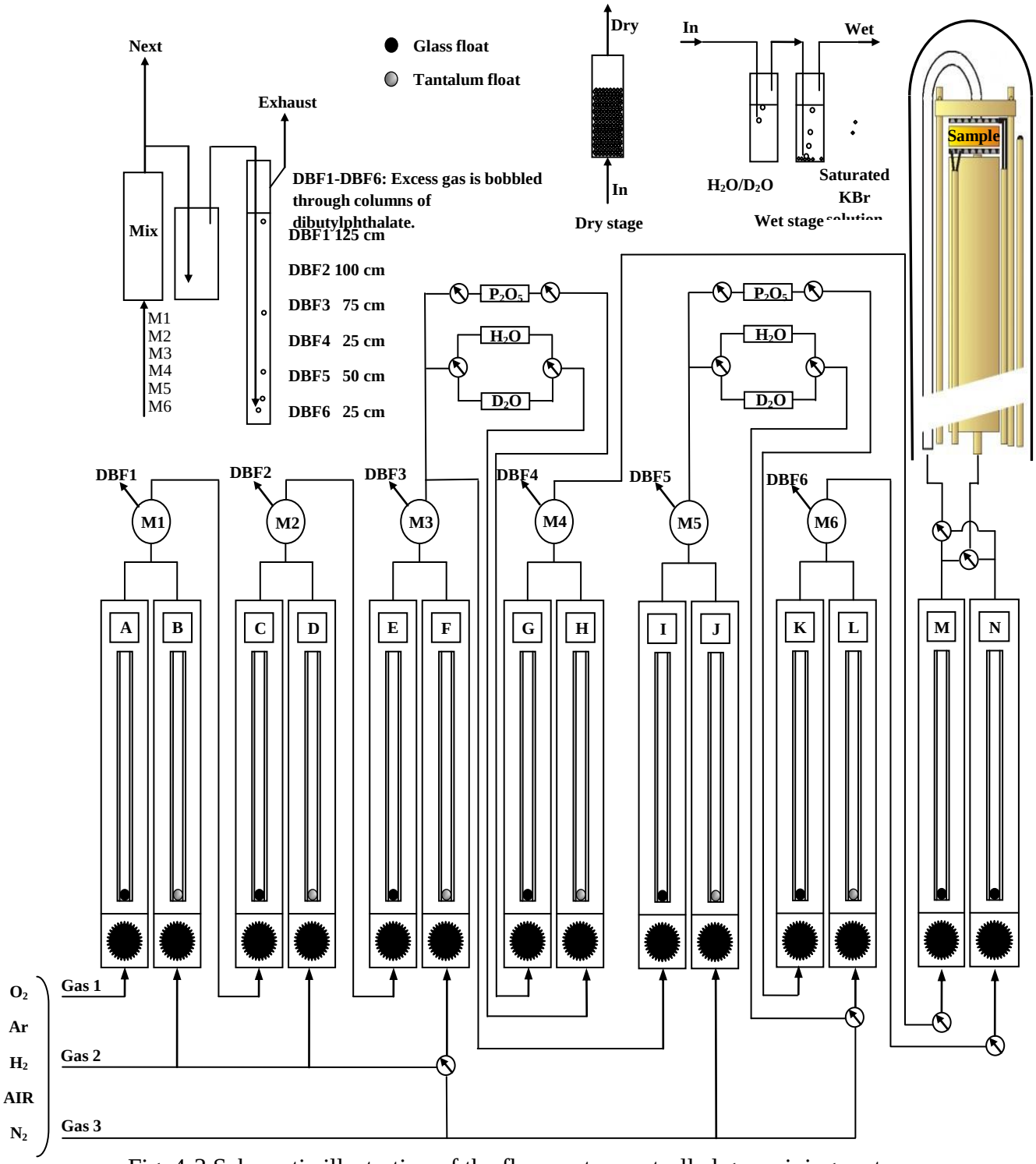

Fig. 4-3 Schematic illustration of the flow meter controlled gas-mixing system

In this gas-mixing system, each mixing unit (M1-M6) has of two flow meters which are equipped with different type of float: a glass float and a tantalum float for each. The gas flow in the tantalum ball flow meter is usually 5-10 times as much as the gas flow in the one with glass ball on the same scale, depending on the different density of the gases. Thus, it is possible to dilute one type of gas (Gas 1) in the ratio 1:10000.

In the first stage, gas1 from flow meter A is mixed with gas 2 from flow meter giving a mixed gas M1, a constant gas flow is directed to flow meter C and mixed with gas 2 from flow meter D, giving a mixture M2. The excess part of M1 is directed to columns contain dibutyl and then into the exhaustion system as waste gas. In the same way, M2 from flow meter E can be mixed with gas 3 from flow meter F giving a gas mixture M3. M3 may be humidified and/or dried before entering flow meter G or H, respectively. The gas flow ratio between flow meters G and H gives the water vapor partial pressure in M4, which enters one chamber of the measurement. M3 (I) could also be mixed with gas 3(J) giving mixtures M5. M5 could thus be humidified and/or dried before entering flow meters K and L, respectively, giving M6. M6 enters the other chamber of the measurement cell.

In this gas-mixing system which contains 6 mixing stages, three different gases could be mixed in the system. The oxygen partial pressure in the measuring cell can be controlled within the range approximately from 1 to 10^{-30} atm by using O_2/Ar, CO/CO_2 and H_2/Ar mixtures depending on the cell temperature. The water partial pressure is controlled within the range approximately from 0 to 2.3×10^{-2} by mixing different proportion of gas dried over P_2O_5 column ($p_{H2O} \approx 2\times10^{-6}$ atm) and gas humidified by bubbling through pure water (or pure heavy water) and then a saturated KBr water solution (or saturated KBr heavy water solution).

The intermediate partial pressures for different gases in different dependencies measurements was calculated with a computer program called “GasMix**”**by NorECs^{TM} by inputting flow meter connection setting, flow meter reading for each flow meter as well as the cell temperature.

4.3.6 Experimental errors analysis

In this work, several devices, connector as well as gas lines are used for electrical measurements. Inevitably, errors are brought into the experimental results, and some of them would influence on the experiment results to a more or less degree. There is little possibility to avoid all of these error sources. However, considerations on these sources are of necessity.

In the measurement cell, the thermocouple was placed approximately 1cm below the specimen which brings a temperature bias at about 2 to 5°C. While, in gas mixing stages, the bias between the values of actual gas flow and readings of flow meters should be awarded. For at high gas flows the bias is expected to be ±5%, and bias would be larger in low gas flow situations [24]. Based on these facts, flow meters are usually used with flow readings ranging from 130-20. Air leakage into the measurement cell would also influence on the electrical measurement result when samples are measured in atmospheres with very low oxygen partial and/or water vapor partial pressure. The uncertainty in geometric factors for ceramic samples should also be considered.

4.3.7 Electrical measurements

The AC conductivity was measurement in the temperature range of 1000°C to 200°C by means of impedance spectroscopy and at a constant frequency of 10 kHz.

The total conductivity as a function of temperature measurement was measured by temperature ramps from 1000°C to 200°C, with a decreasing temperature of 12°C/hour both in dry oxygen and wet oxygen separately.

The total conductivity as a function of oxygen partial pressure was measured in wet (0.025atm H_2O) O_2/Ar mixtures for oxidizing conditions and wet (0.025atm H_2O) H_2/Ar mixtures for reducing conditions and as a function of the water vapor partial pressure at temperatures of 1000°C, 800°C and 600°C separately. The oxygen partial pressure was controlled by mixing O_2 with Ar for oxidizing conditions and H_2 with Ar for reducing conditions.

The total conductivity as a function of water partial pressure in oxidizing conditions was measured from 1000°C to 400°C in 100°C intervals. The water vapor pressure was controlled by mixing different proportion of dried oxygen and wet oxygen.

H^+/D^+ isotope effects on the total conductivity were investigated under oxidizing conditions (H_2 + 0.025 atm H_2O and D_2 + 0.025 atm D_2O).

4.4 Experimental data analysis

Impedance spectra were deconvoluted with the “Equivalent Circuit” (“EQUIVCRT” or “EQC”) software by Bernhard Boukamp of the University of Twente, the Netherlands.

Conductivity dependency fitting was carried out with a computer programme “Table curve 2D®” by Systat Software Inc. The total conductivity, temperature, doping concentration, oxygen partial pressure and water vapor pressure were used as input data for a nonlinear last square fitting procedure. The fitting procedure used Equation to fit the measured total conductivity measured under different conditions. The accepter doping concentration was assumed constant which is equal to the nominal doping. The fitting determined the thermodynamic factors for the defect reaction equilibrium by input data.

Nonlinear last square fitting of the experimental data was carried out with a computer programme describe in earlier chapter. Thus, the entropy and enthalpy of the defect reaction equilibrium between oxygen vacancies, water vapor, protons and mobilities for charge carriers are determined.

5. Results and Discussion

5.1 Sample preparation

β-$La_{1.96}Sr_{0.04}WO_{6-\delta}$ obtained by wet chemical synthesis method has relatively higher density than that synthesized in the traditional solid state synthesis method. Also, it is observed that, the sintering temperature for powder obtained is lower than those by solid state method. And it is also observed that, powders synthesized by wet chemical method have the tendency to melt at 1350°C.

Sample 3 and sample 4 were sintered at 1500°C (it would have the tendency to melt at 1550°C), which is different from the sintering temperature of 1350 °C reported by Tyulin A.V. and et al. [25]. The difference between sintering temperatures might come from different ways of powder synthesis, Tyulin A.V. and et al. used solid state synthesis method[25] by mixing stoichiometric amount of Nd_2WO_6 and Lu_2WO_6, while wet chemical synthesis method is used in this work.

Sample number	Sample component	relative density
Sample 1	β-$La_{1.96}Sr_{0.04}WO_{6-\delta}$	85 %
Sample 2	β-$La_{1.96}Sr_{0.04}WO_{6-\delta}$	90 %
Sample 3	$Nd_{1.176}Ca_{0.024}Lu_{1.176}Mg_{0.04}WO_{6-\delta}$	95 %
Sample 4	$Nd_{1.176}Ca_{0.04}Lu_{1.176}WO_{6-\delta}$	95 %

5.2 Structural characterization

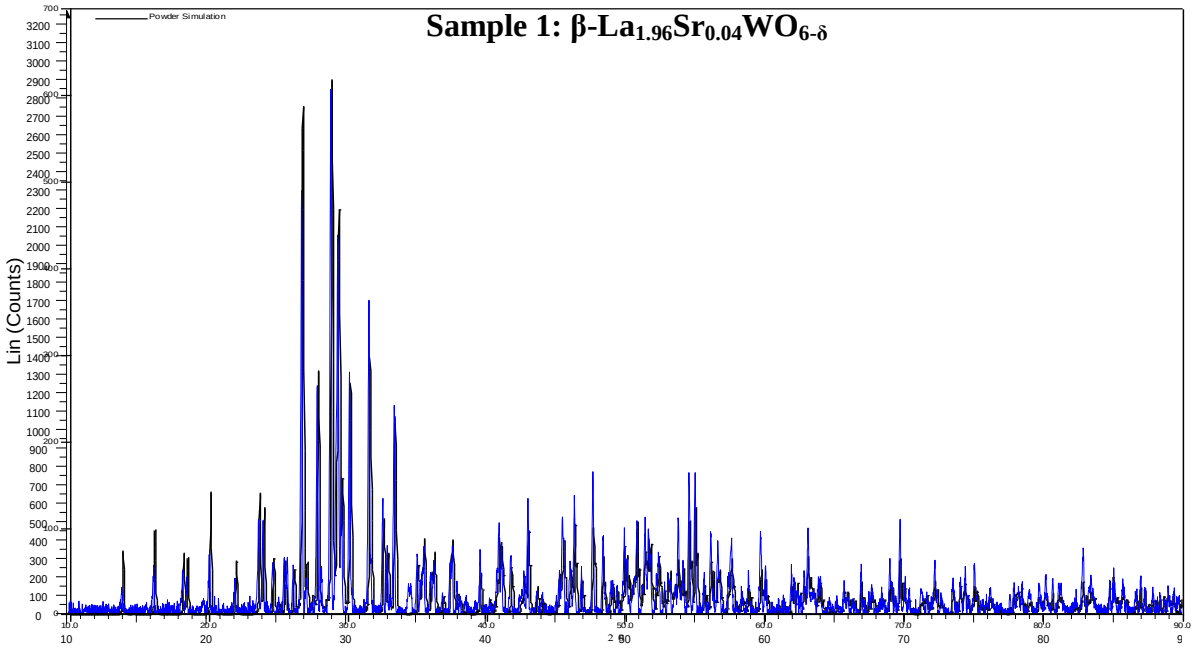

Figure 5-1 XRD result compared with reference **[7, 22]**

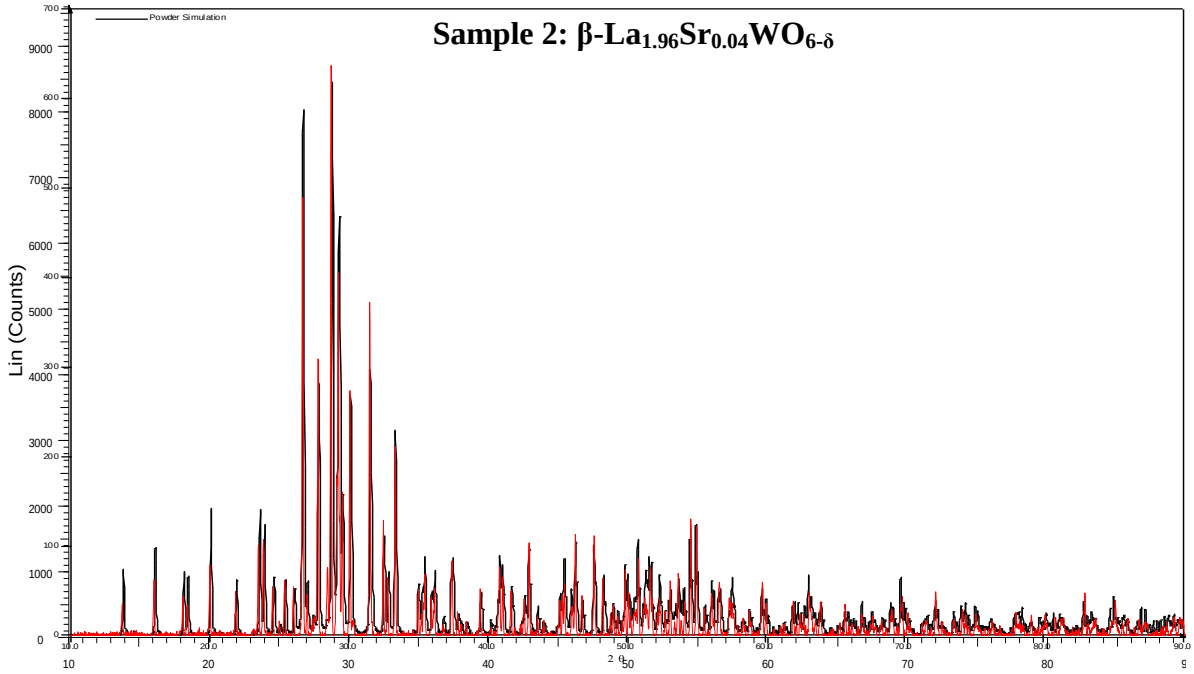

Figure 5-2 XRD result compared with reference **[7, 22]**

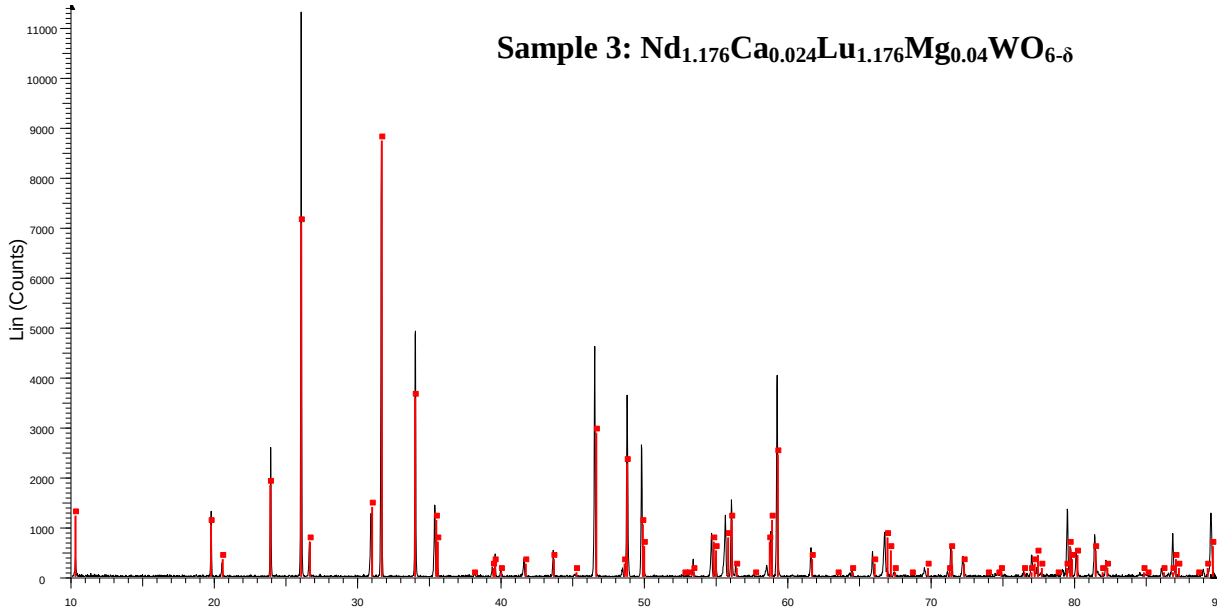

Figure 5-3 XRD result compared with reference**[25]**

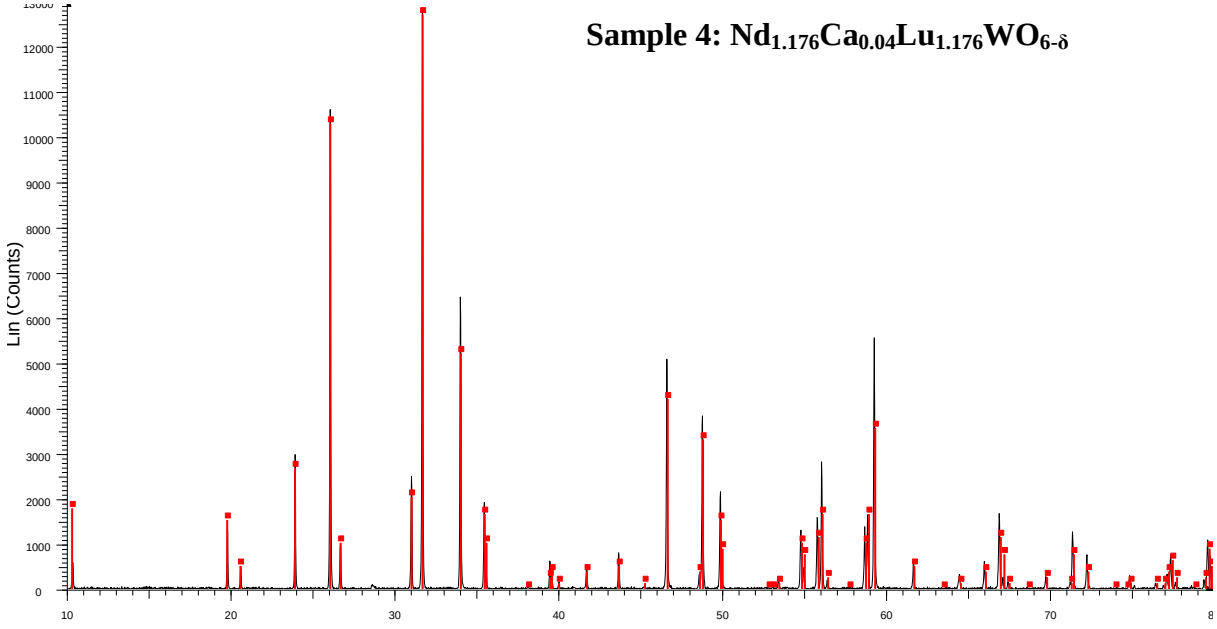

Figure 5-4 XRD result compared with reference **[25]**

As we can see, the power XRD pattern of these four samples are in accordance with refence data.

5.3 Microstructural characterization

Sample 2: β-$La_{1.96}Sr_{0.04}WO_{6-\delta}$

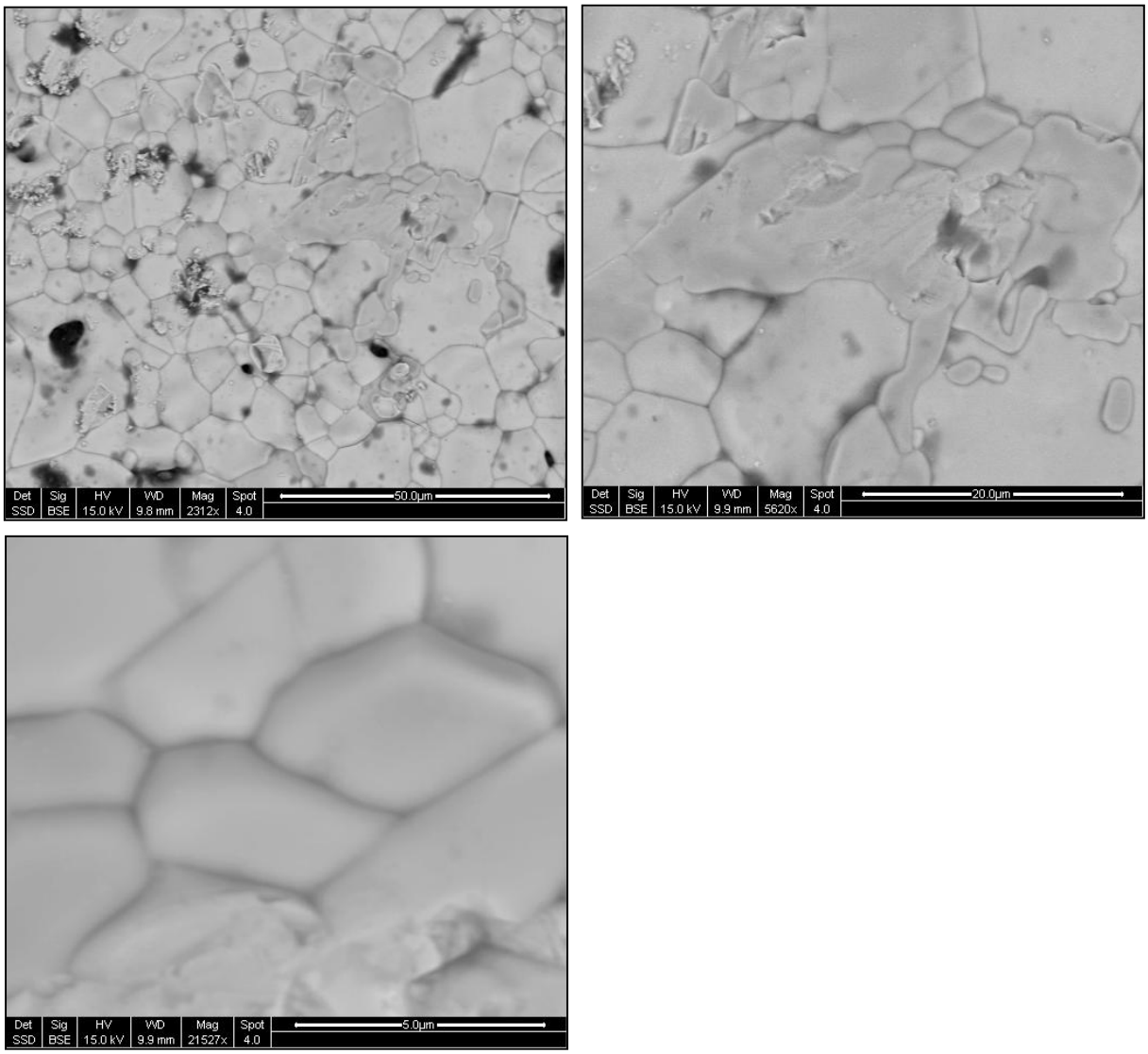

Figure 5-5 SEM micrographs from the back-scattered electron detector

No significant second phase was observed on the surface of sample 2 with SEM. The grain size are approximately 5 to 10 μm.

Sample 3 $Nd_{1.176}Ca_{0.024}Lu_{1.176}Mg_{0.04}WO_{6-\delta}$

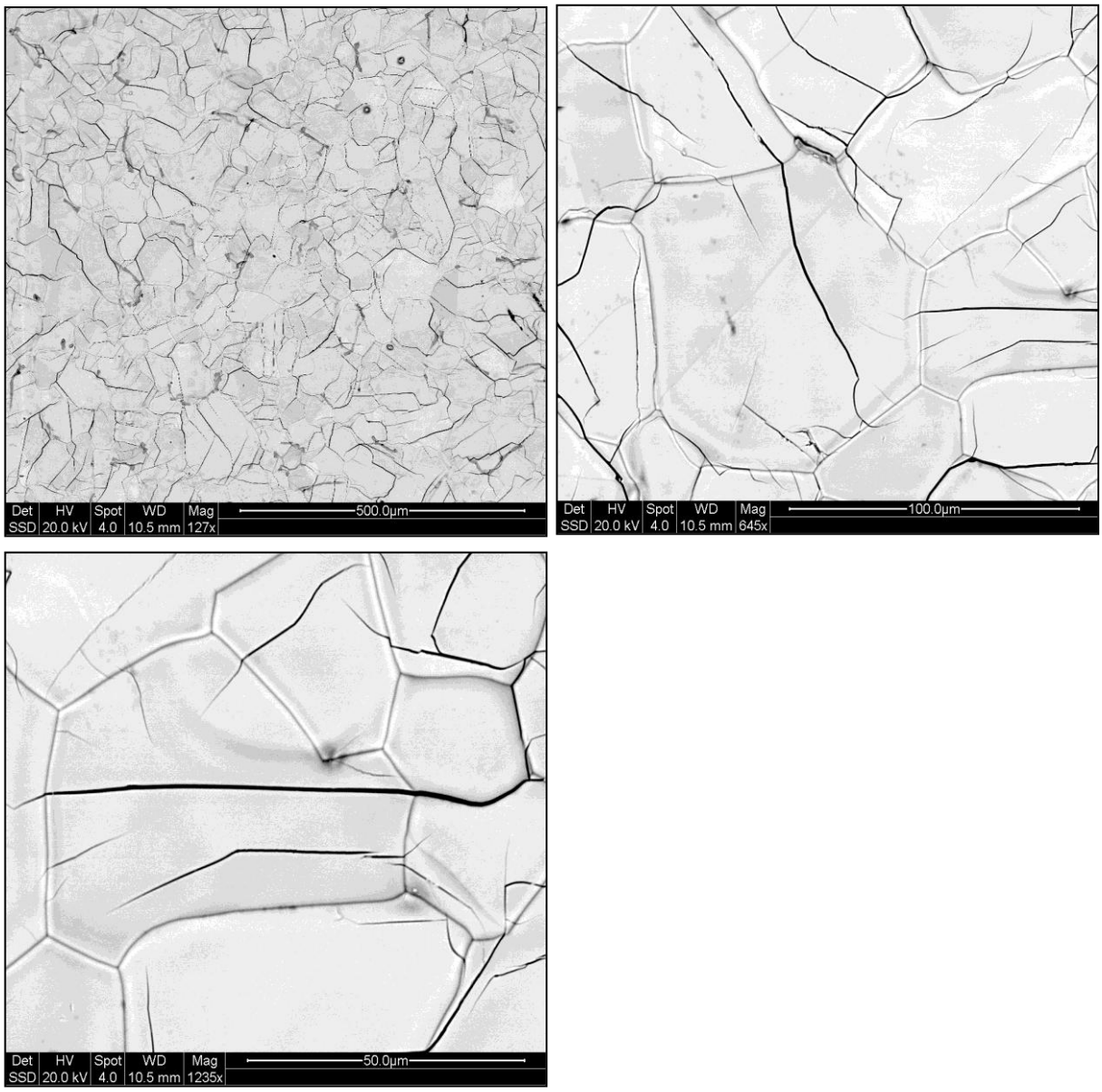

Figure 5-6 SEM micrographs from the back-scattered electron detector

No significant second phase was observed on the surface of sample 3 with SEM. The grains are much larger compared with sample 2. The diameter of grains is approximately 25 to 50 µm.

Sample 4: $Nd_{1.176}Ca_{0.04}Lu_{1.176}WO_{6-\delta}$

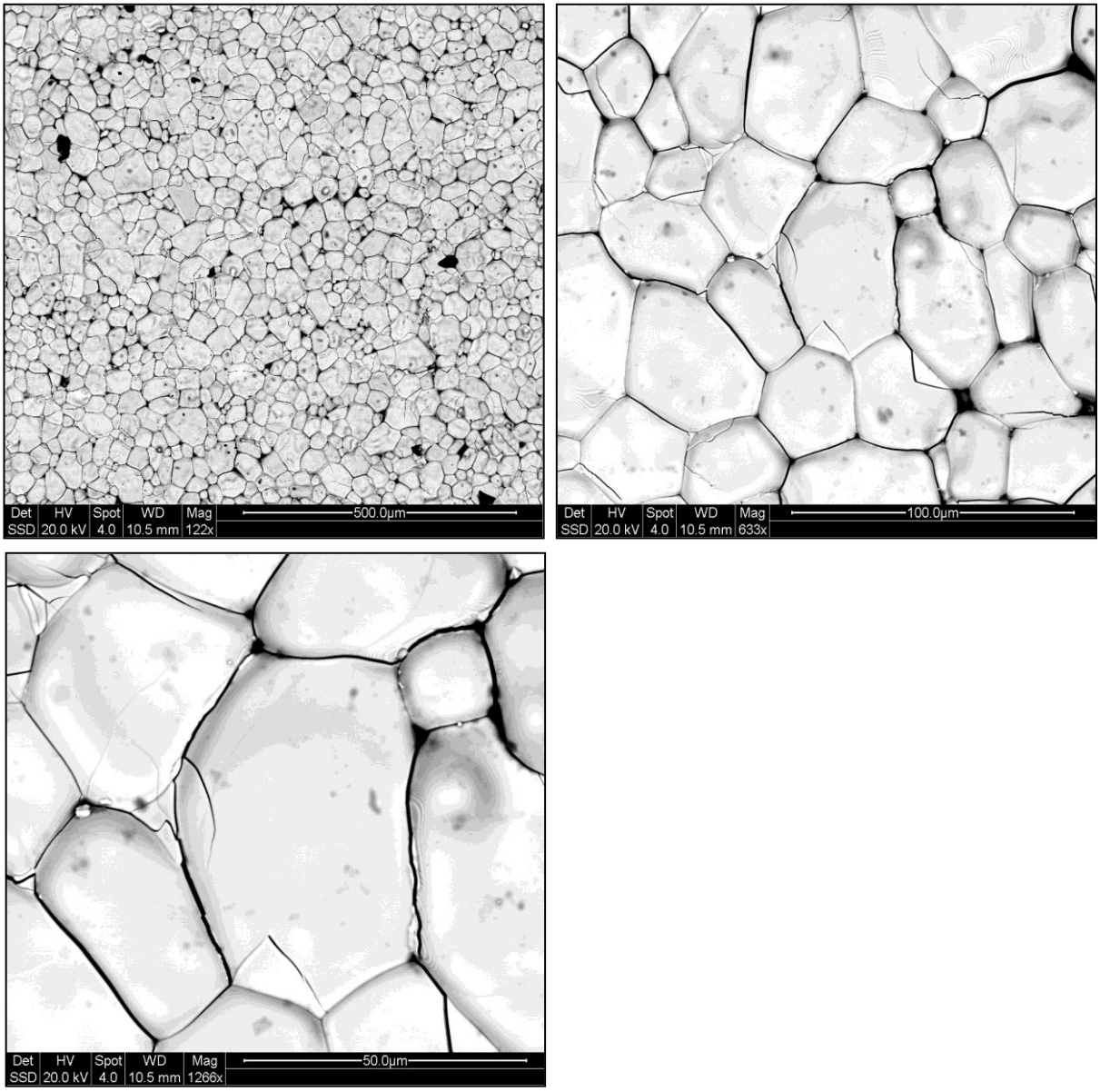

Figure 5-7 SEM micrographs from the back-scattered electron detector

No significant second phase was observed on the surface of sample 4 with SEM. The diameter of grains is approximately 15 to 40 μm.

5.4 Impedance spectra analysis

The impedance spectra of the material were recorded at different temperatures and atmospheres during all measurements in order to distinguish the contributions of conductivity from material bulk, grain boundary and electrode. A typical impedance spectrum is shown below:

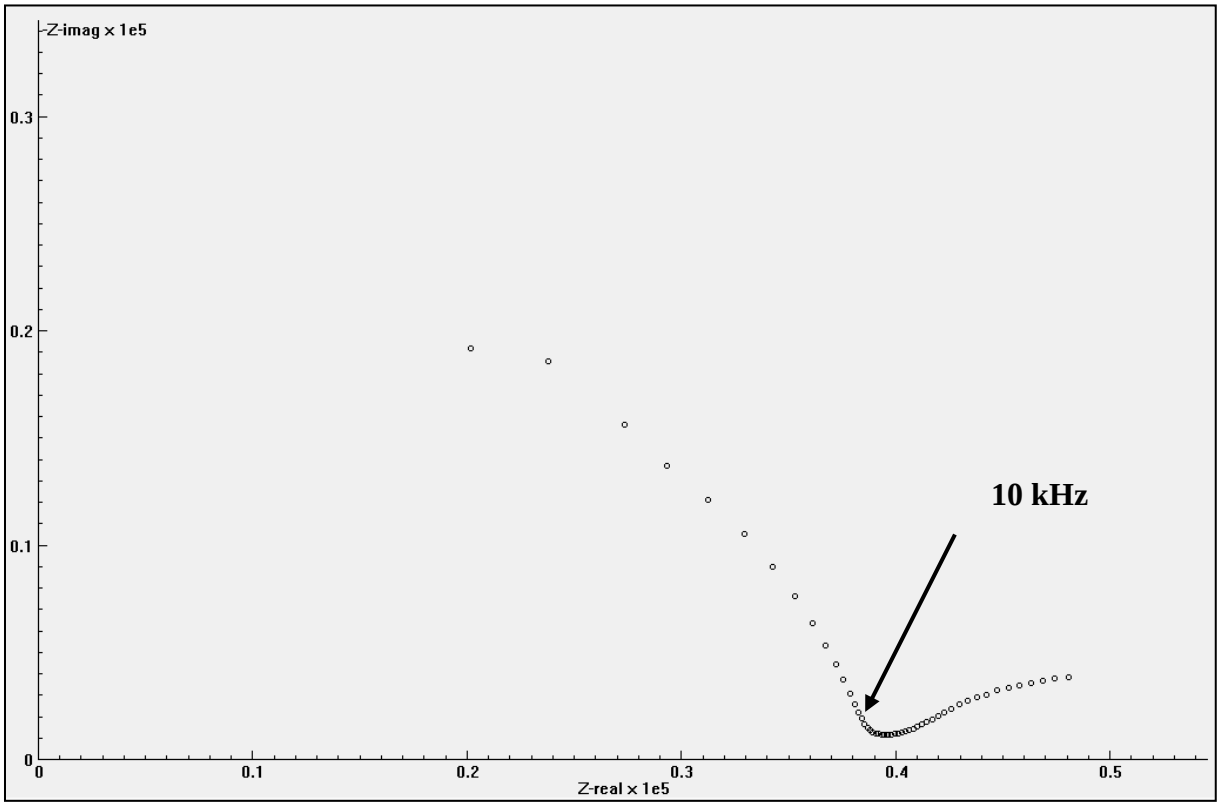

Fig.5-8 AC impedance spectrum at 600°C in wet oxygen with 3.64×10^{-3} atm H_2O for β-$La_{1.96}Sr_{0.04}WO_{6-\delta}$

As we can see, there are two semi-circles shown in the spectrum which correspond to material bulk and grain boundary property indicated by the calculated capacitances of the two arcs and then the values of capacitance is compared with Table 1. And all the calculated results all show that the bulk part was measured when 10k Hz of frequency was applied for the AC current.

5.5 Total conductivity as a function of the inverse absolute temperature

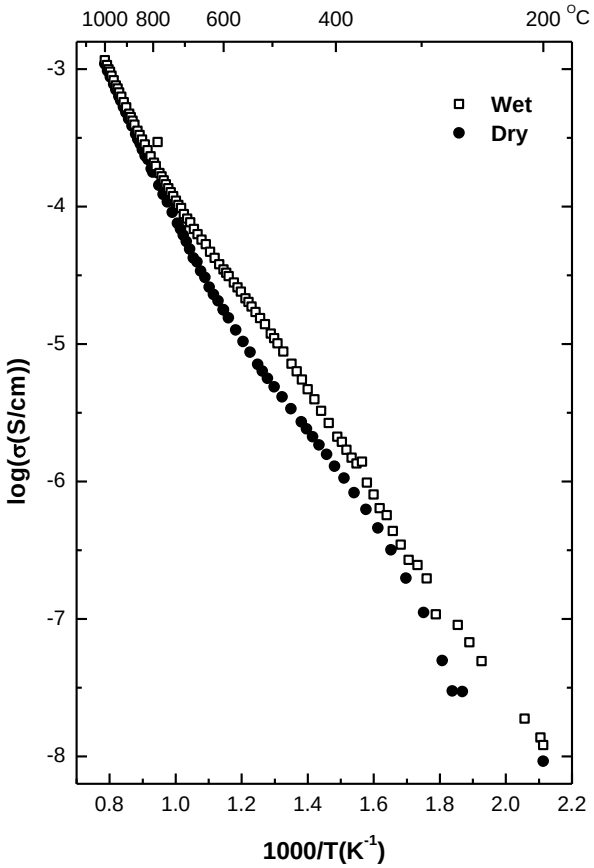

Fig. 5-9 Total conductivity as a function of the inverse absolute temperature for β-$La_{1.96}Sr_{0.04}WO_{6-\delta}$ measured in O_2-0.025 H_2O atm and O_2- ~ 3×10^{-5} from 200 °C to 1000°C

At temperatures above 700°C, the conductivities in wet and dry conditions are similar. At lower temperatures, conductivity in wet condition shows higher values than that in dry condition. The difference of conductivity between wet and dry become more significant with decreasing temperatures until approximately 400°C, and then the two cures is close again. We attribute the similar conductivities between wet and dry below 400°C due to the measuring limit of the impedance spectrometer. The clear water effect gives a first indication of proton conduction at lower temperatures.

5.5 Total conductivity as a function of the oxygen partial pressure

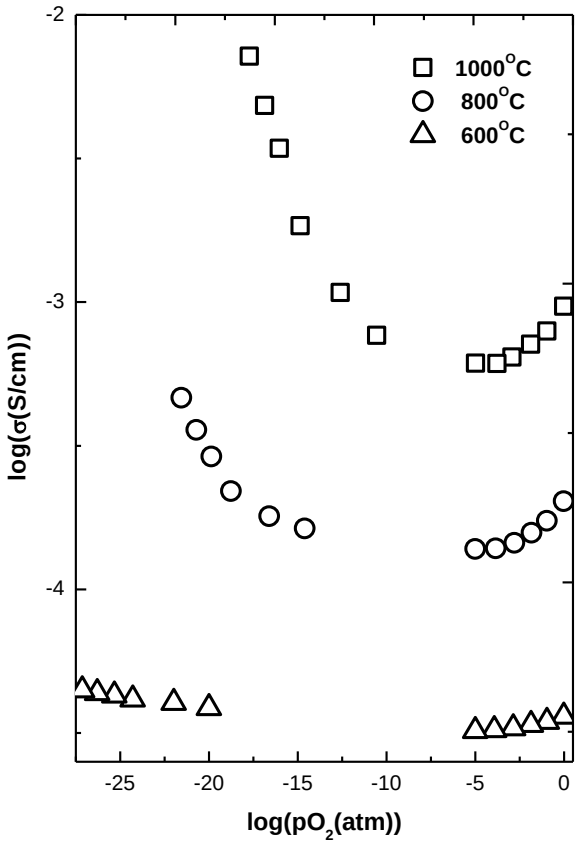

Fig. 5-10 Total conductivity as a function of the oxygen partial pressure at differerrnt temperatures from 600°C to 1000°C for β-$La_{1.96}Sr_{0.04}WO_{6-\delta}$ from wet H_2 to wet O_2 conditions

As we can see from Fig. 5-9, the material shows n-type electronic conductivity at low pO_2 regime and p-type electronic conductivity at high pO_2 regime in general. The conductivity cure bend significantly at the 1000°C indicating significant contributions form electronic conductivity and the contribution become less significant with decreasing temperature. At 600°C, the electrical conduction is negligible because of the almost independent conductivity behavior on pO_2 form H_2 to O_2. The conductivity at the lower temperatures is therefore dominated by the ionic conductivities. The pO2 dependency cure as well as the pH_2O dependency date will be utilized for deriving partial conductivities and thermodynamic parameters for charged species transport.

5.6 Total conductivity as a function of the water vapor partial pressure

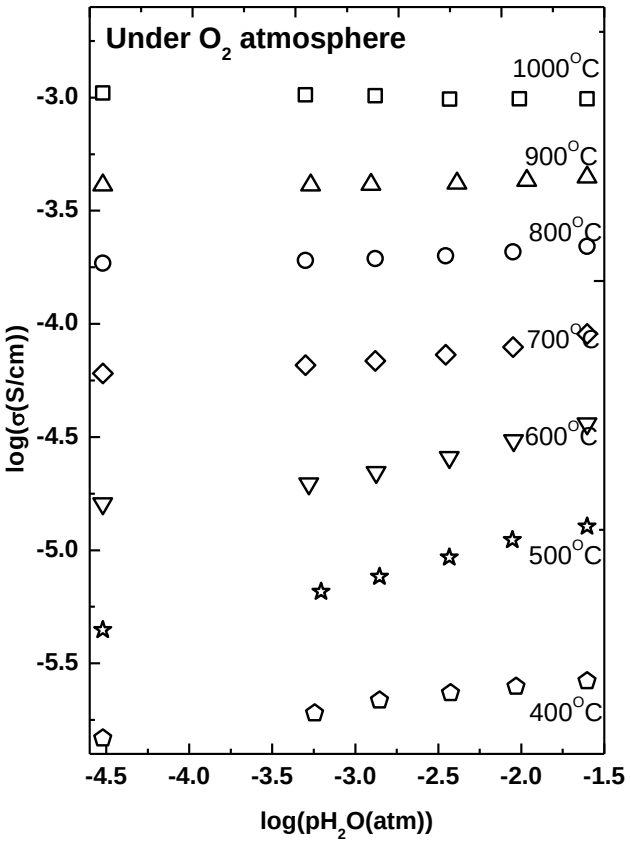

Fig. 5-11 Total conductivity as a function of water vapour partial pressure in oxygen at different temperatures from 400°C to 1000°C for β-$La_{1.96}Sr_{0.04}WO_{6-\delta}$

As we can see form Fig.5-10 that the conductivity increases with increasing water vapour partial pressure at intermediate temperature. Above 800°C, the increasing in conductivity with increased water vapour partial pressure become insignificant, indicating less proton conductivity contribution to the total conductivity.

However, at the lowest temperature, 400°C, conductivity first increases with increasing water vapour partial pressure and then it becomes independent on the water partial pressure when the water content approaches to ¼.

This indicates that the material is wholly hydrated which implies that the proton concentrations will independent on the water vapour partial pressure. The slop of the curves at intimidate temperature is approximately 1/4 which is smaller that the expected 1/2 with proton conduction dominating.

The reason of the lower dependency could be due to the mixed conductivity property that both oxide ion and proton conductivity contribute significantly to the total conductivity. P-type electronic conductivity in this case would be negligible according to the negligible pO_2 dependency at 600°C as shown in fig.5-9. At 600°C the conductivity point in wet O_2 corresponds well with the above data in pO_2 dependency indicating an equilibrium state for both measurements.

5.7 Isotope effect of conductivity

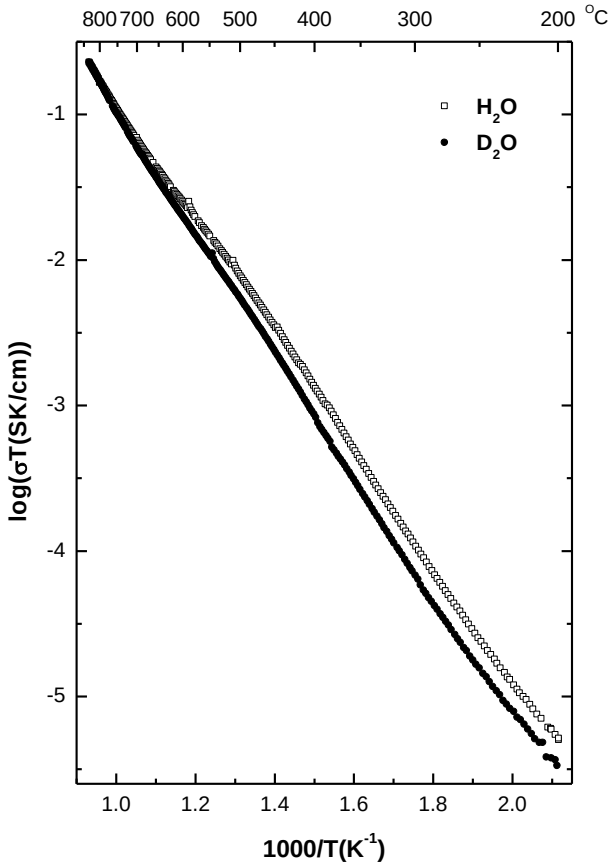

Fig. 5-12 Total conductivity as a function of the inverse absolute temperature for β-$La_{1.96}Sr_{0.04}WO_{6-\delta}$ measured in O_2-0.025 H_2O atm and O_2-0.025 D_2O from 200 °C to 800°C

The conductivity isotope effect was clearly observed below 600°C under oxygen atmosphere as shown in Fig.5-11 at temperatures above 800°C, the conductivity cures in H_2O and D_2O are overlapped meaning the insignificant proton conductivity contribution.

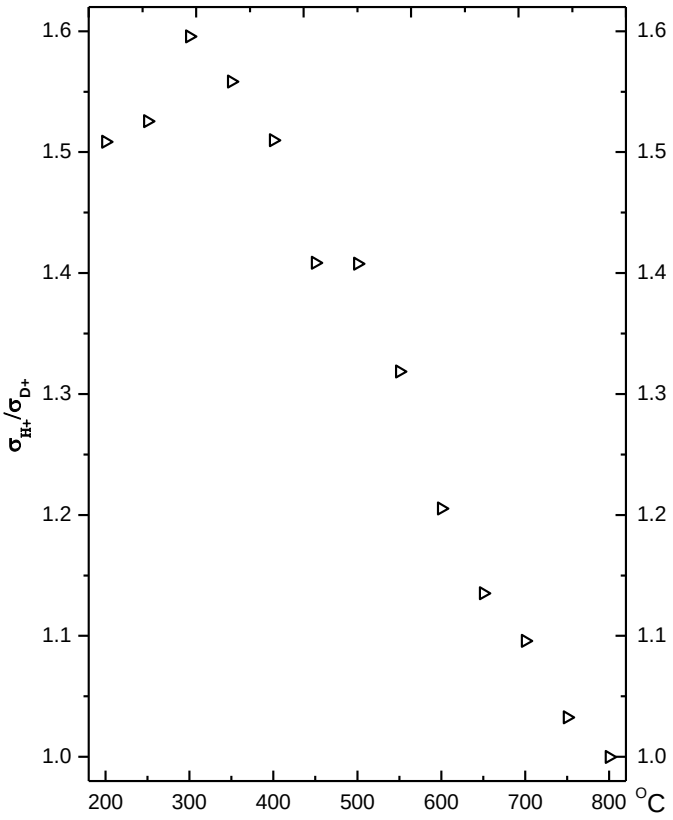

Fig. 5-13 $\sigma H_+/\sigma_{D+}$ at different temperatures from 200°C to 800°C

The value of σ_{H+}/σ_{D+} from 200 °C to 600°C is around ~1.4 suggesting a high contribution of proton conductivity assuming a classical approach of H^+ and D^+ defects migration as well possible tunneling effect happen at low temperature[26]. The high value of σ_{H+}/σ_{D+} around 300 °C suggests tunneling effect which happen at low temperatures. However the isotope effect is qualitatively determining method for proton conductivity, therefore the estimation for proton conductivity contribution could have some uncertainty. Nevertheless, the clear isotope effect at lower temperatures gives a strong indication of proton conduction in the material.

5.9 Conductivity fitting

Nonlinear last square fitting of the experimental data was carried out with a computer programme "Table curve 2D®" as describe in earlier chapter. Thus, the entropy and enthalpy of the defect reaction equilibrium between oxygen vacancies, water vapor, protons and mobilities for charge carriers are determined.

Activation energy for oxygen vacancy at low temperatures

At intermediate and lower temperature region ranging from 700°C to 400°C, Arrhenius diagram was plotted for activation engery of oxygen ion

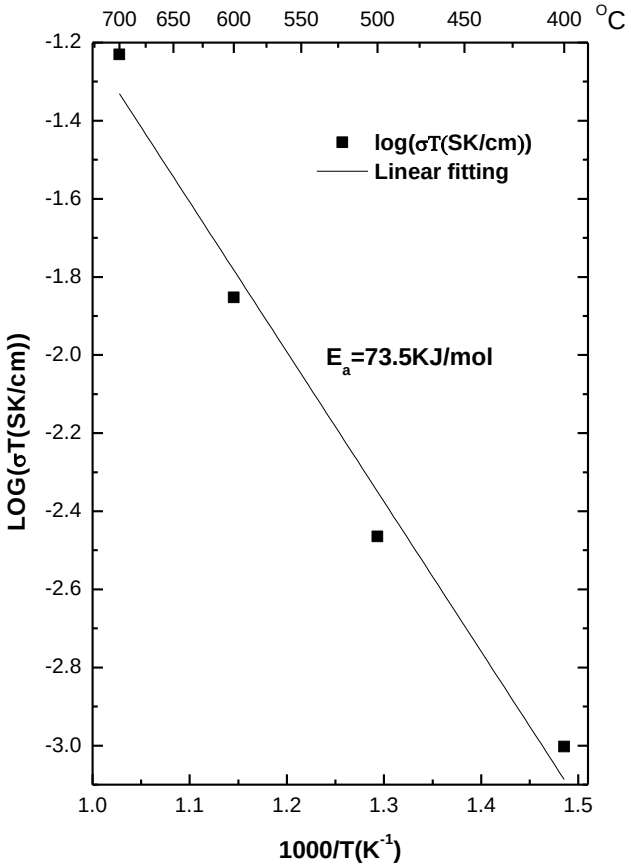

Fig. 5-14 Arrhenius diagram for oxygen ion activation energy from 400°C to 700°C

The calculated activation energy for oxygen ion conductivity is 73.5KJ/mol with equation (2-32)

Activation energy for oxide ion condution at high temperatures

From fig.5-10, the plateau regions are dominated by oxygen ion conductivity. Within this region, the conductivity of oxygen ion at 1000°C, 800°C and 600°C plotted by using Arrhenius type diagram was shown as fig.5-14

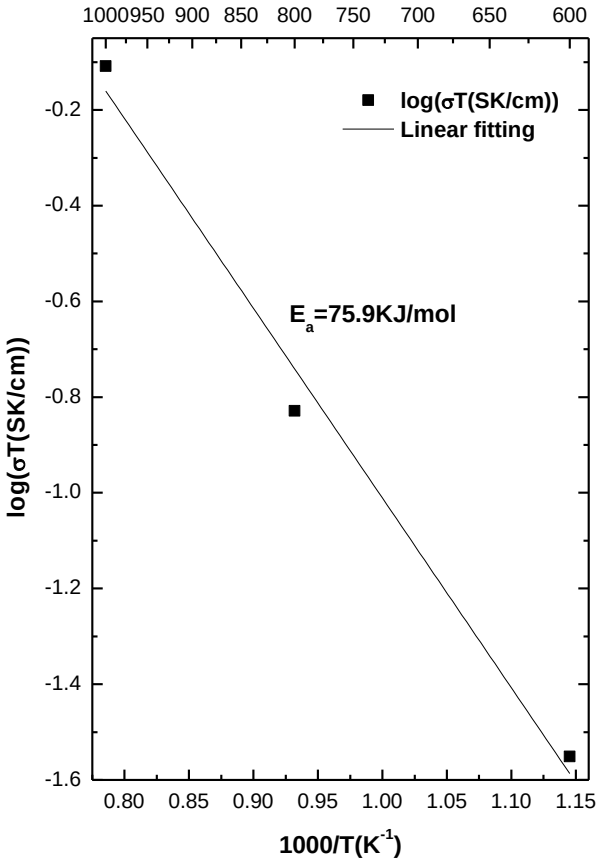

Figure 5-14 Arrhenius diagram for oxygen ion activation energy at temperature from 600°C to 1000°C

Equation (2-32) was used for calculation; the calculated activation energy for oxygen ion conductivity is 75.9KJ/mol, which fits activation energy at lower temperature regions quite well.

Activation energy for proton at low temperatures

For region from 200°C to 350°C, the sample could be regarded as fully hydrated.

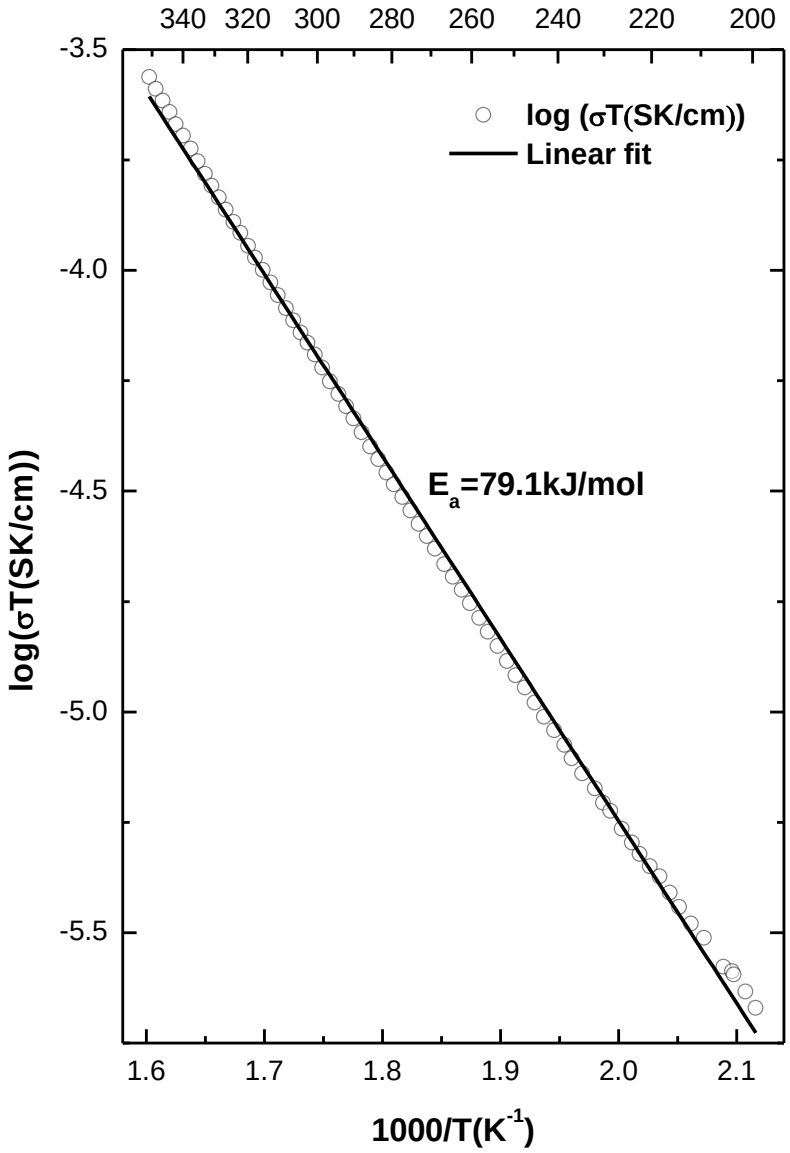

Figure 5-14 Arrhenius diagram for proton jump at temperature from 200°C to 350°C

Equation (2-32) was used for calculation

The activation energy for proton is 79.1kJ/mol

Pre-exponential factor for oxygen vacancy

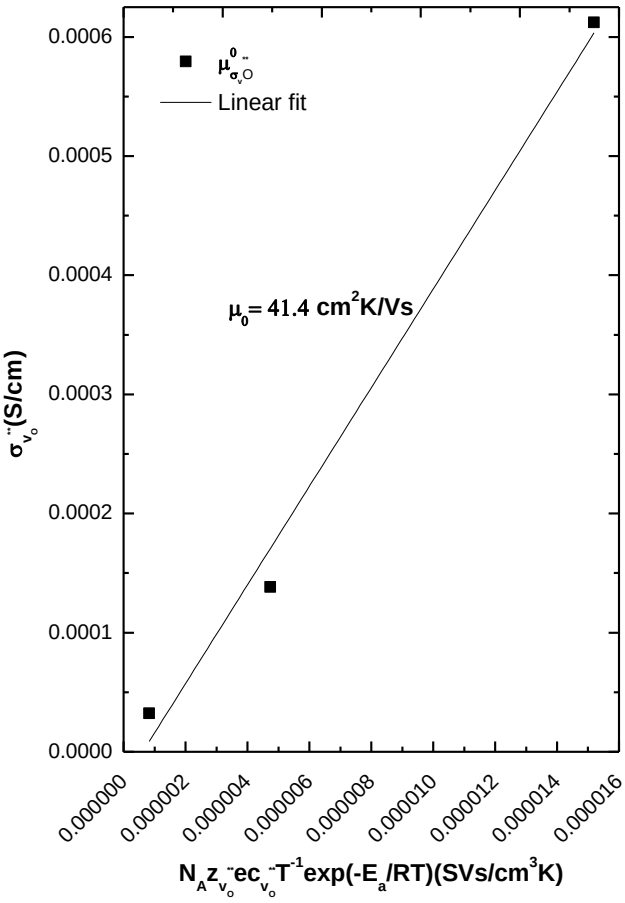

Fig. 5-15 Linear fitting for preexponential mobility for oxygen vacancy

Equation (2-19) was used for calculation

μ_{vo}=41.4 cm_2 K/Vs

Conductivity with pH_2O dependency fitting at 400°C

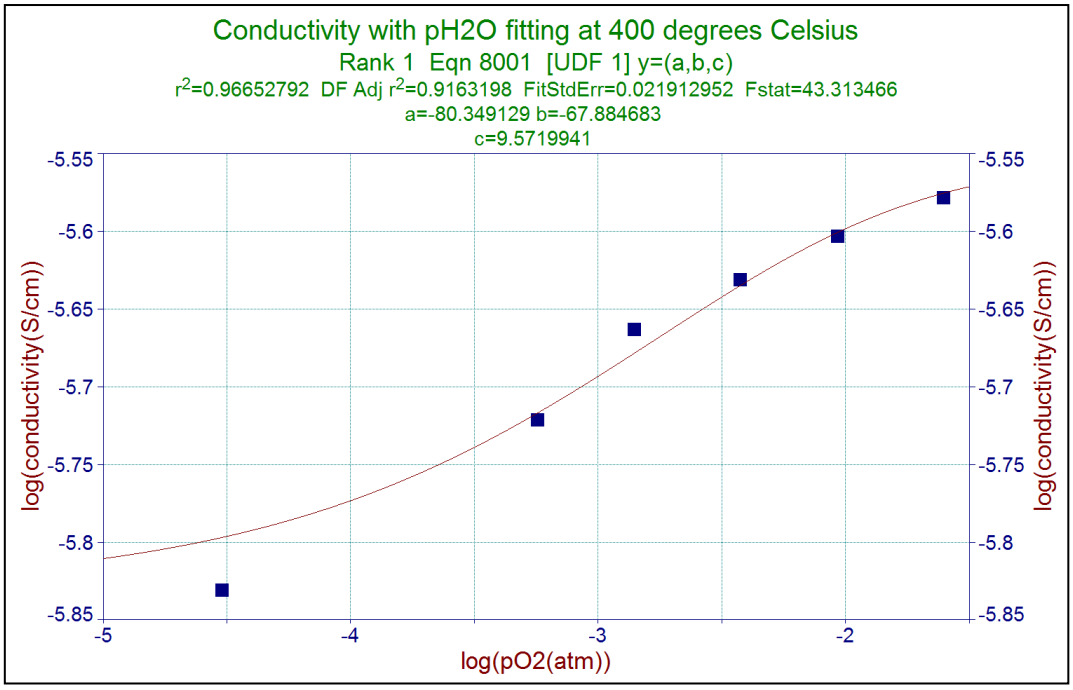

Figure 5-18 Conductivity dependency with pH_2O fitting at 400°C

Equations (2-19) – (2-13) are used for fitting

ΔS_H= -80.35J/molK ΔH_H=-67.88KJ/mol μ_H=9.57 cm^2/Vs

Conductivity with pH_2O dependency fitting at 500°C

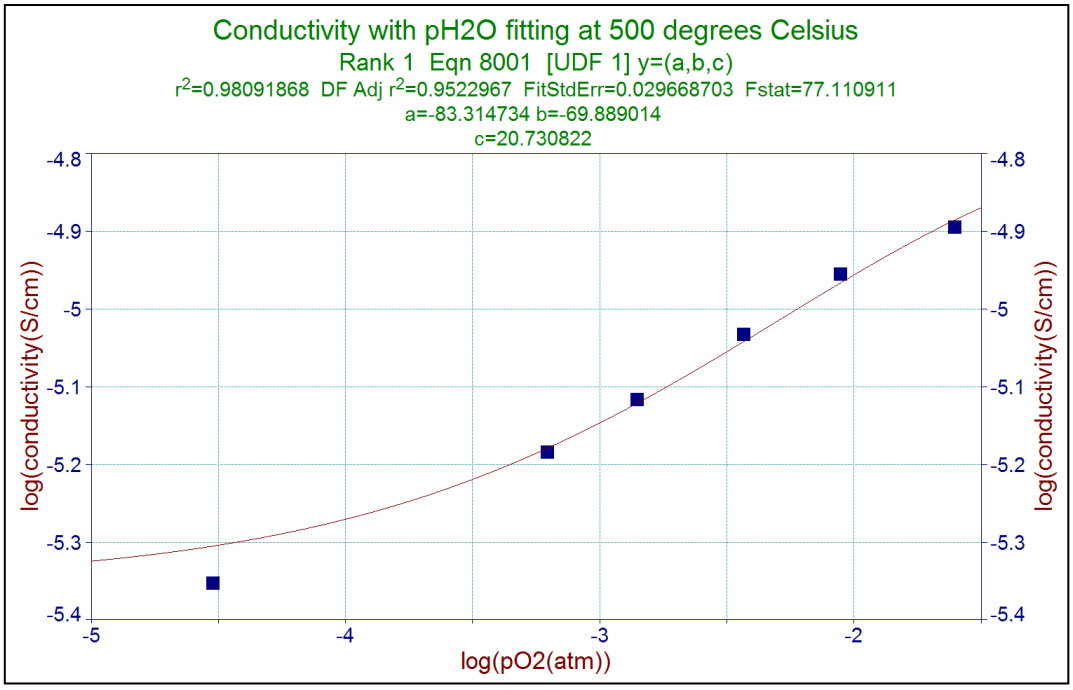

Figure 5-19 Conductivity dependency with pH_2O fitting at 500°C

Equations (2-19) – (2-13) are used for fitting

ΔS_H= - 83.31J/molK, ΔH_H= - 69.89KJ/mol, μ_H = 20.73 cm^2/ Vs

Conductivity with pH_2O dependency fitting at 600°C

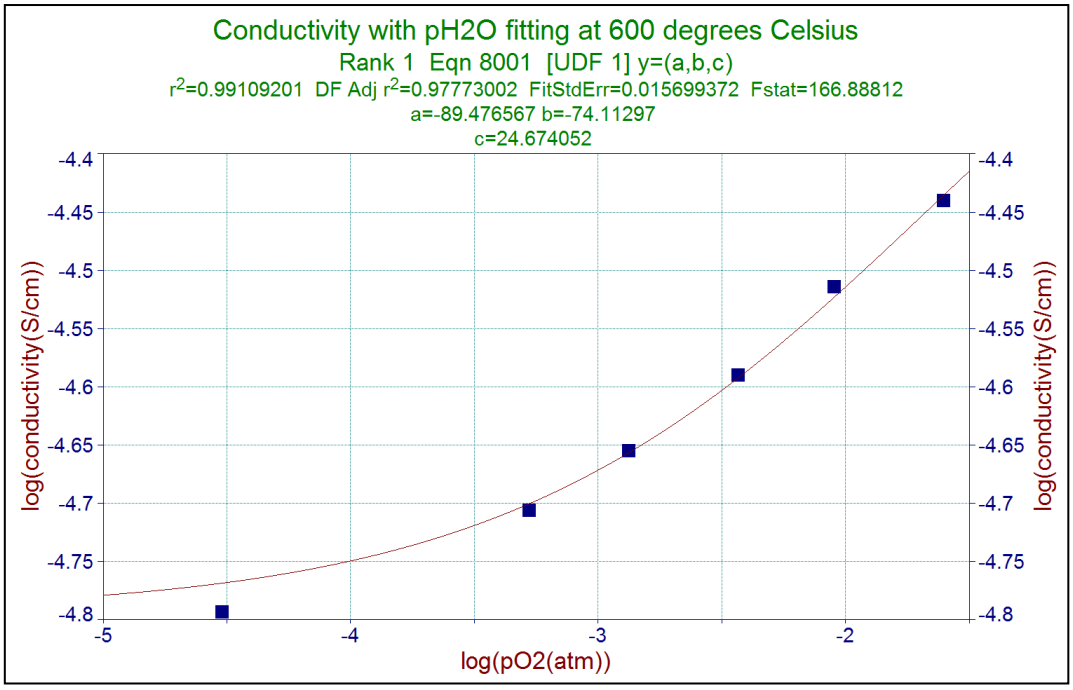

Figure 5-20 Conductivity dependency with pH_2O fitting at 600°C

Equations (2-19) – (2-13) are used for fitting

ΔS_H= - 89.48J/molK ΔH_H = -74.11KJ/mol μ_H = 24.67 cm^2/ Vs

Conductivity with pH_2O dependency fitting at 700°C

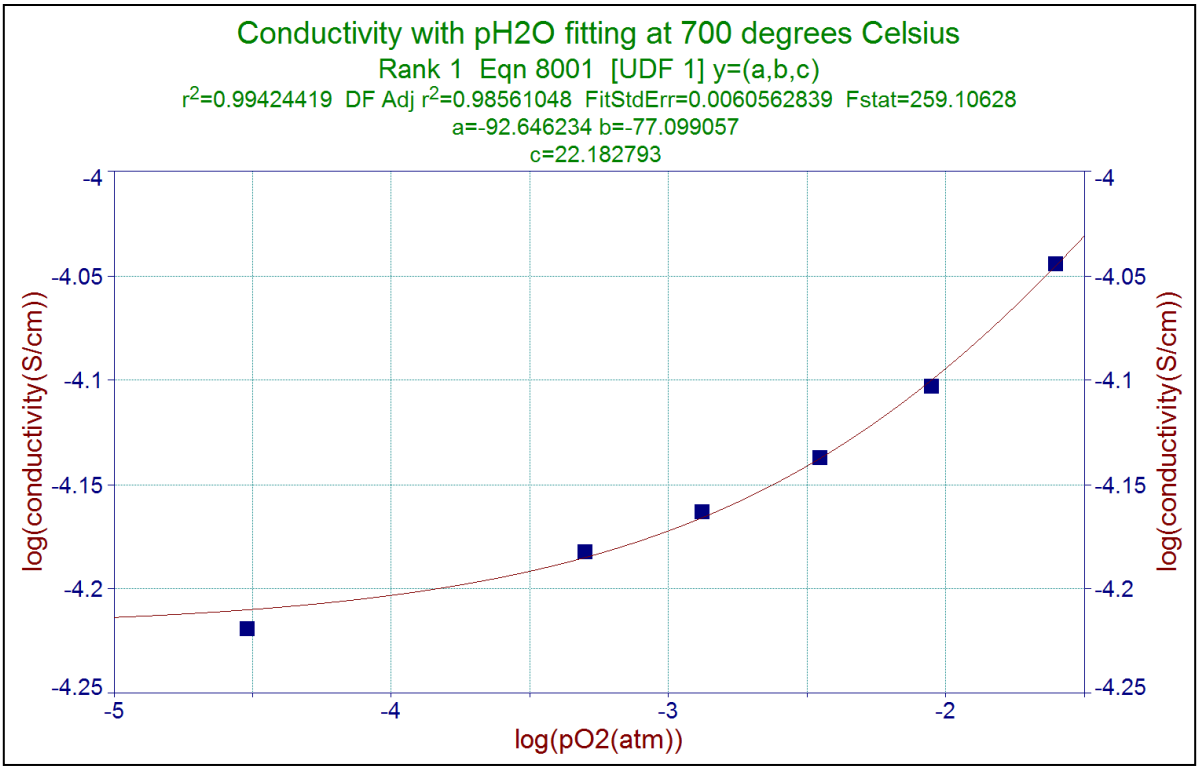

Figure 5-21 Conductivity dependency with pH_2O fitting at 700°C

Equations (2-19) and (2-13) are used for fitting

ΔS_H= -92.65J/molK ΔH_H=-77.10KJ/mol μ_H=22.18 cm^2/ Vs

Conductivity with pH_2O dependency fitting at 800°C

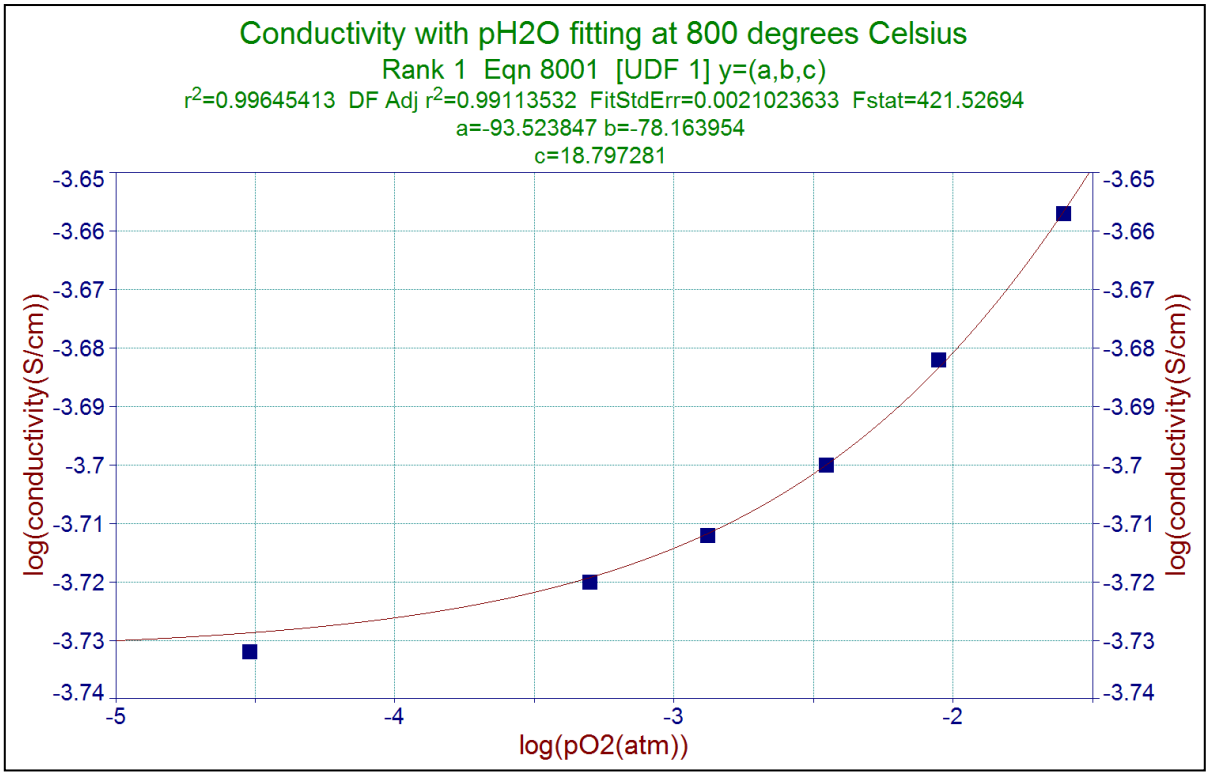

Figure 5-22 Conductivity dependency with pH_2O fitting at 800°C

Equations (2-20), (2-21), (2-22), (2-23) and (2-24) are used for fitting

ΔS_H= -93.52J/molK ΔH_H=-78.16KJ/mol μ_H=18.80 cm^2/ Vs

Total (conductivity*T) as a function of the inverse absolute temperature for $Nd_{1.176}Ca_{0.04}Lu_{1.176}WO_{6-\delta}$

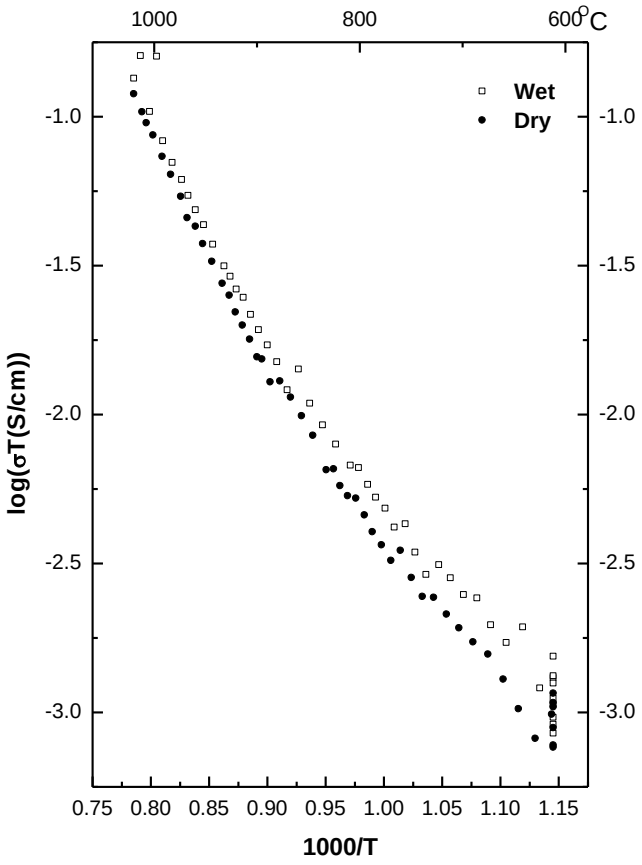

At temperatures below 1000°C, conductivity in wet condition shows higher values than that in dry condition. The difference of conductivity between wet and dry become more significant with decreasing temperatures until approximately 600°C. However the eletrical tranport behavior can not be observed due to the limit of the

6. Conclusion

Transport property on β-$La_{1.96}Sr_{0.04}WO_{6-\delta}$

The total conductivity as a function of inverse temperature in wet and dry oxygen gives the first indication of proton conduction. The total conductivity at wet oxygen is always higher than that in dry oxygen.

The total conductivity as a function of water vapor partial pressure gives the second indication of proton conduction. The proton conduction in the material is also indicated by the clear isotope effects observed in this work.

The material shows mixed conduction properties which are mixed oxide ion- and electronic-conductivity at higher temperatures and mixed oxide ion- and proton- conductivity at lower temperature.

The thermodynamic parameters derived by a conductivity fitting are summarized in the following table.

Table 6-1 Thermodynamic parameters for hydration and proton transport

ΔS_{hyd}[J/mol K]	ΔH_{hyd}[kJ/mol]	$\mu_0(H)$[cm^2/Vs]	ΔH_m[kJ/mol]
-87 +/- 7	**-72 +/- 5**	**17 +/- 8**	**79.1**

References

1. Colomban, P., *Proton Conductors Solids, membranes and gels - materials and devices*. Chemistry of Solid State Materials (No. 2)2008: Cambridge University Press.
2. Haugsrud, R. and C. Kjølseth, *Effects of protons and acceptor substitution on the electrical conductivity of La6WO12.* Journal of Physics and Chemistry of Solids, 2008. **69**(7): p. 1758-1765.
3. Haugsrud, R., et al., *Mixed Ionic and Electronic Conductivity of Undoped and Acceptor-Doped $Er6WO_{12}$.* Journal of The Electrochemical Society, 2007. **154**(1): p. B77-B81.
4. Haugsrud, R., *Defects and transport properties in Ln_6WO_{12} (Ln=La, Nd, Gd, Er).* Solid State Ionics, 2007. **178**(7–10): p. 555-560.
5. Magraso, A., et al., *New crystal structure and characterization of lanthanum tungstate "La_6WO_{12}" prepared by freeze-drying synthesis.* Dalton Transactions, 2009(46): p. 10273-10283.
6. Solís, C., et al., *La5.5WO12-δ Characterization of Transport Properties under Oxidizing Conditions: A Conductivity Relaxation Study.* The Journal of Physical Chemistry C, 2011. **115**(22): p. 11124-11131.
7. Chambrier, M.H., et al., *Ab-initio structure determination of β-La_2WO_6.* Journal of Solid State Chemistry, 2009. **182**(2): p. 209-214.
8. Norby, T., *KJM5120-Defects and transport in crystalline solids*, UiO.
9. Norby, T., *Proton conduction in oxides.* Solid State Ionics, 1990. **40–41, Part 2**(0): p. 857-862.
10. Macdonald, J.R. and W.B. Johnson, *Fundamentals of Impedance Spectroscopy*, in *Impedance Spectroscopy*2005, John Wiley & Sons, Inc. p. 1-26.
11. Norby, T., *KJM-MENA4010 Electrical measurements*.
12. D.C. Sinclair, F.D.M., A.R. West, International Ceramics, 2000. **2**: p. 33-37.
13. Norby, T., *Solid-state protonic conductors: principles, properties, progress and prospects.* Solid State Ionics, 1999. **125**(1–4): p. 1-11.
14. Norby, T. and N. Christiansen, *Proton conduction in Ca- and Sr-substituted LaPO4.* Solid State Ionics, 1995. **77**(0): p. 240-243.
15. K. Amezawa, Y.K., Y. Tomii, and N. Yamamoto, *High Temperature Protonic Conduction in LaP_3O_9.* Electrochem. Solid-State Lett., 2004. **7**: p. A511-4.
16. Amezawa, K., et al., *High temperature protonic conduction in LaBO3 with the aragonite-type structure.* Solid State Ionics, 2004. **175**(1–4): p. 575-579.
17. Amezawa, K., et al., *High temperature protonic conduction in Sr-doped La_2Si2O_7.* Solid State Ionics, 2005. **176**(3–4): p. 341-347.
18. Haugsrud, R. and T. Norby, *Proton conduction in rare-earth ortho-niobates and ortho-tantalates.* Nat Mater, 2006. **5**(3): p. 193-196.
19. Shimura, T., S. Fujimoto, and H. Iwahara, *Proton conduction in non-perovskite-type oxides at elevated temperatures.* Solid State Ionics, 2001. **143**(1): p. 117-123.
20. al., W.X.a.e., *Structure and transport properties in un-doped and acceptor-doped "Gd_6WO_{12}"*.
21. M. Yoshimura, A.R., Mater. Res. Bull., 1976. **11**(2): p. 151-158.
22. Allix, M., et al., *Synthesis and Structure Determination of the High Temperature Form of La_2WO_6.* Crystal Growth & Design, 2011. **11**(11): p. 5105-5112.
23. www.norecs.com.
24. Wood, J.R., *Defects and conductivity in Sr-doped $LaNb_3O_9$.* Master thesis, UiO, 2007: p. 63-64.
25. Tyulin A.V., E.V.A., Trunov V.K., *Polymorphism of oxytungstates TR_2WO_6. Structure of tetragonal $Nd_{1.2}Lu_{0.8}WO_6$.* Sov. Phys. Crystallogr., 1989. **34**: p. 46–49.
26. Nowick, A.S. and A.V. Vaysleyb, *Isotope effect and proton hopping in high-temperature protonic conductors.* Solid State Ionics, 1997. **97**(1–4): p. 17-26.